

國立臺灣大學理學院天文物理所

碩士論文

Institute of Astrophysics

College of Science

National Taiwan University

Master Thesis

南極超高能宇宙微中子陣列之事件重建模擬

Simulation of the Event Reconstruction of  
Ultra High Energy Neutrino with Askaryan Radio Array



Shang-Yu Sun

指導教授：陳丕燾 博士

Advisor: Pisin Chen, Ph.D.

中華民國 99 年 1 月

January, 2010

# Acknowledgement

Thanks for my adviser, Prof. Pisin Chen, who makes so many efforts so that Taiwan team can participate in ARA, such a great international scientific project. This is not only an interesting research topic for me, but also a good chance to experience international collaboration. Every time in meeting, he can always give inspirational comments from his scientific intuition we admire so much. Thanks for Dr. Melin Huang's very careful instructions. She always gives out her opinions and writes down clearly item by item with her beautiful handwriting. Thanks for Dr. Jiwoo Nam's experienced guiding. His teaching was systematic. He gave almost the whole structure of simulation.

Thanks for Professor Guey-Lin Lin. He leads the cosmic neutrino group, and it is pleasant to discuss with him. Thanks for Professor Min-Zu Wang. He was my adviser and also found me his experienced student to help me use GEANT4. Thanks for the computers in room 802, the High Performance Grid Computing provided by National Taiwan University, and the National Center for High-performance Computing, all of which helped me complete the intensive computing for this work.

Thanks for Chien-Wen Chen's opinions for Chapter Two and his unique sense and sensibility. Thanks for Chih-Ching Chen's practical and smart opinions. Thanks for Feng-Yin Chang. Her live "O Mio Babbino Caro" refreshed me and brought me away from the darkness in r802. Thanks for Chia-Yu Hu's company along these years and useful advices. Thanks for Ruo-Yu Shang's heart-warming chocolate in the winter of my life as a graduate student. Thanks for Pao-Yu Wang, Shi-Hao Wang, Hsin-Yi Tu, Chiu-Chuan Yao, and Tien-Chi Liu's lifesaving encouraging words. Thanks for Chien-Ting Chen's slide template. Thanks for Christine Gruber for helping me tell the wrong from the right whenever black is white or day is night.

Thanks for Shang-Jhen Li for teaching me the preliminary work for using PBS. Thanks for Yin-Jen Lin, who help me to learn PBS commands for submitting jobs to the computer-grids. Thanks for all the secretaries' efforts so that academic events can go smoothly. Thanks for my sister, parents, grandparents, and all mountain guys' everlasting support.

## 摘要

南極超高能宇宙微中子陣列是一個已被提案的科學計畫，旨在藉由無線電波段之契忍可夫輻射偵測超高能宇宙微中子，以了解宇宙加速器之起源及演化。為評估藉由超高能宇宙微中子指回產生它們的宇宙加速器的可能性，我們採用偏離角來描述此可能性：在百分之一的信心水準下，有九成的宇宙超高能微中子在地球端的觀測偏離小於一度。而為了使南極超高能宇宙微中子陣列的幾何設計能最佳化，我們研究了幾何設計與微中子角度解析度和偵測效率關係，同時也考慮了不同程度的背景雜訊所帶來的影響。我們發現無線電站相距 1.6 公里且天線相距 40 公尺能讓陣列表現最佳。

關鍵字：南極超高能宇宙微中子陣列，超高能/GZK/宇宙微中子，無線電波偵測超高能宇宙微中子，微中子角度解析度，事件重建之模擬，超高能宇宙微中子之偏離角。



# Abstract

Askaryan Radio Array (ARA) is a large-scale radio Cherenkov observatory which scientists propose to develop in Antarctica, aiming for discovering the origin and evolution of the cosmic accelerators that produce the highest energy cosmic rays, by means of observing the ultra high energy (UHE) cosmogenic neutrinos. To determine whether it is probable to use UHE neutrinos for pointing back to the cosmic accelerators, an assessment of the deviation angles of these neutrinos has been made, and its conclusion is that the probability of observing the neutrino deviation angle within 1 degree is 90%. To optimize ARA's angular resolution of the incoming UHE neutrinos, which is also essential to point back, the relation between the reconstruction capabilities of ARA and its design is studied. It is found that with the noise effect taken into account, in order to make this neutrino angular resolution as good as possible and detection efficiency as high as possible, the optimal choice for ARA geometry would be the station spacing of 1.6 km and the antenna spacing of 40 m.

Key words: Askaryan Radio Array (ARA), UHE/GZK/cosmosgenic/cosmic neutrinos, radio detection of UHE neutrinos, UHE neutrino angular resolution, resolution of UHE neutrino incoming direction, simulation of event reconstruction, deviation angles of GZK neutrinos

# Contents

|          |   |           |
|----------|---|-----------|
| <b>1</b> | <b>Introduction</b>   | <b>12</b> |
| 1.1      | The Mystery of Cosmic Accelerators . . . . .                      | 12        |
| 1.2      | Greisen-Zatsepin-Kuzmin(GZK) Cutoff and GZK Process . . . . .     | 15        |
| 1.3      | UHE Neutrino: Key to the Mystery of Cosmic Accelerators . . . . . | 17        |
| 1.4      | Detection of UHE neutrinos . . . . .                              | 18        |
| 1.5      | Radio Detection Experiments of UHE Neutrino: ARA Design Concepts  | 21        |
| <b>2</b> | <b>Deviation Angle of Cosmogenic Neutrino</b>                     | <b>24</b> |
| 2.1      | A New Quantity to Measure the Deviation: $\theta_{max}$ . . . . . | 24        |
| 2.2      | Proton Energy Loss Length . . . . .                               | 26        |
| 2.3      | Angular Diameter Distance . . . . .                               | 29        |
| 2.4      | GZK Neutrino Flux from Proton Propagation . . . . .               | 31        |
| 2.5      | Conclusion of the Assessment . . . . .                            | 33        |
| <b>3</b> | <b>Simulation Method</b>  | <b>36</b> |
| 3.1      | Setting Array Geometry . . . . .                                  | 36        |
| 3.2      | Event Production . . . . .  | 37        |

|          |   |           |
|----------|---|-----------|
| 3.3      | Radio Cherenkov Wave from the shower location to Antennas . . . . .                           | 40        |
| 3.4      | Determination of Arrival Time Difference and Pulse Voltage . . . . .                          | 43        |
| 3.5      | Reconstruction of Neutrino Moving Directions . . . . .  | 44        |
| <b>4</b> | <b>Results</b>  | <b>46</b> |
| 4.1      | Resolutions of Arrival Time Difference and Pulse Voltage . . . . .                            | 46        |
| 4.2      | Resolutions of Shower Location, RF Wave Direction, and Neutrino<br>Moving Direction . . . . . | 48        |
| 4.3      | Optimization of ARA . . . . .   | 52        |
| <b>5</b> | <b>Summary</b>  | <b>68</b> |
|          | <b>Bibliography</b>   | <b>70</b> |



# List of Figures

|     |  |    |
|-----|--|----|
| 1.1 | <i>This is a CR energy spectrum of <math>E^2dN/dE</math> for protons, antiprotons, electrons, and positrons.</i>   | 13 |
| 1.2 | <i>Energy spectrum of UHECR observation and GZK neutrino prediction.</i>   | 16 |
| 1.3 | <i>Nucleon energy vs. traveling distance.</i>  | 17 |
| 1.4 | <i>Range and energy limitation of photons or protons as astrophysical messengers.</i>  | 19 |
| 1.5 | <i>Askaryan effect in ice: field strength vs frequency in radio band and radiative Cherenkov power vs. shower energy.</i>  | 21 |
| 1.6 | <i>Askaryan effect in ice: angular dependence of Cherenkov field strength.</i>   | 22 |
| 2.1 | <i>Illustration of how protons and GZK neutrinos travel from AGN to the Earth.</i>   | 26 |
| 2.2 | <i>Proton energy loss length, <math>L_{loss}</math> as a function of <math>z + 1</math>, where the proton energy is set as <math>2 \times 10^{20} eV</math>, where <math>z</math> is the redshift.</i> | 29 |
| 2.3 | <i>Angular diameter distance as a function of <math>z + 1</math>.</i>  | 30 |
| 2.4 | <i>Maximum deviation angle of a GZK neutrino, <math>\theta_{max}</math>, as a function of <math>z + 1</math>.</i>  | 31 |

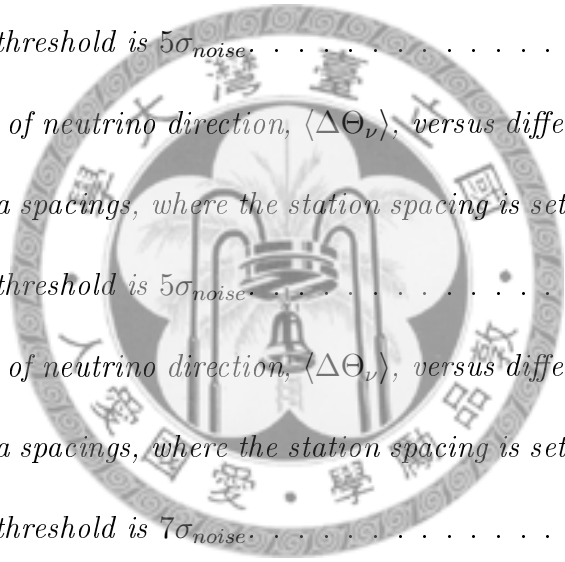
|     |  |    |
|-----|--|----|
| 2.5 | <i>The local GZK neutrino flux per <math>(z+1)</math> at the energy of <math>10^{19}</math> eV . . . . .</i>                           | 33 |
| 2.6 | <i>GZK neutrino flux as a function of its maximum deviation angle. . . . .</i>   | 34 |
| 2.7 | <i>Accumulative probability of observing neutrinos under the maximum deviation angle ranging from zero to a certain angle. . . . .</i> | 35 |
| 3.1 | <i>The geometry of the distribution and their coordinates. . . . .</i>   | 37 |
| 3.2 | <i>ARA antenna cluster geometry in a station, where there are twelve antennas, indicated by green squares. . . . .</i>                 | 38 |
| 3.3 | <i>The shower location field and the 37 ARA stations. . . . .</i>  | 39 |
| 3.4 | <i>Simulated RF waveform before reaching antennas, where the magnitude normalized to 1. . . . .</i>                                    | 41 |
| 3.5 | <i>Illustration of a radio Cherenkov wave, from the shower location to the antenna. . . . .</i>  | 42 |
| 3.6 | <i>An example waveform with noise. . . . .</i>   | 43 |
| 4.1 | <i>Resolution of time. . . . .</i>   | 47 |
| 4.2 | <i>Resolution of voltage. . . . .</i>  | 47 |
| 4.3 | <i>Illustration of the reconstructed shower location (in red) and the generated one (in green). . . . .</i>                            | 48 |
| 4.4 | <i>Resolution of shower location in x axis. . . . .</i>  | 49 |
| 4.5 | <i>Resolution of shower location in y axis. . . . .</i>  | 49 |
| 4.6 | <i>Resolution of shower location in z axis. . . . .</i>  | 50 |
| 4.7 | <i>Illustration of the reconstructed RF wave direction (in red) and the generated one (in green). . . . .</i>                          | 51 |



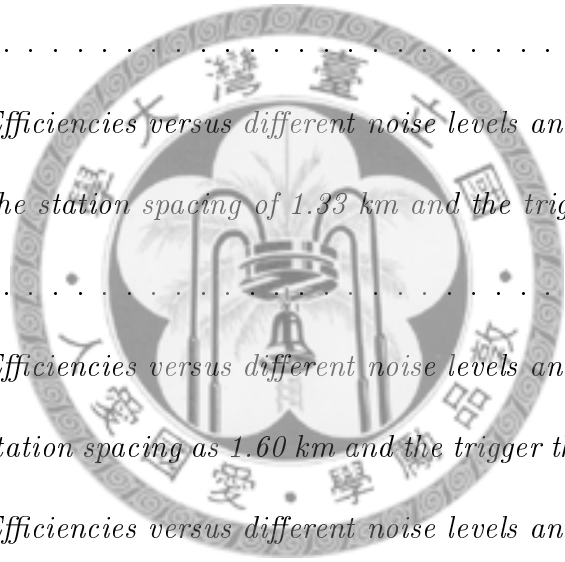


|      |   |    |
|------|---|----|
| 4.8  | <i>Resolution of RF wave direction in zenith angle. . . . .</i>   | 51 |
| 4.9  | <i>Resolution of RF wave direction in azimuthal angle. . . . .</i>  | 52 |
| 4.10 | <i>Illustration of the reconstructed neutrino moving direction (in red)<br/>and the generated one (in green). . . . .</i>   | 53 |
| 4.11 | <i>Resolution of neutrino moving direction in zenith angle. . . . .</i>   | 53 |
| 4.12 | <i>Resolution of neutrino moving direction in azimuthal angle. . . . .</i>  | 54 |
| 4.13 | <i>Distribution of the separation angle between the generated <math>\nu</math> direction<br/>and the reconstructed one. The average of this angle is taken for the<br/>comparison of the neutrino angular resolution in this analysis. . . . .</i>                    | 54 |
| 4.14 | <i>Resolutions of neutrino direction, <math>\langle \Delta\Theta_\nu \rangle</math>, versus antenna spacings<br/>and station spacings. . . . .</i>  | 56 |
| 4.15 | <i>3D display of resolutions of neutrino direction, <math>\langle \Delta\Theta_\nu \rangle</math> (in unit of<br/>degree), versus antenna spacings and station spacings. . . . .</i>  | 57 |
| 4.16 | <i>Detection efficiencies versus antenna spacings and station spacings. . . . .</i>   | 57 |
| 4.17 | <i>Resolutions of neutrino direction, <math>\langle \Delta\Theta_\nu \rangle</math>, versus different noise levels<br/>and antenna spacings, where the station spacing is set at 1.33 km and<br/>the trigger threshold is <math>3.5\sigma_{noise}</math>. . . . .</i> | 59 |
| 4.18 | <i>Resolutions of neutrino direction, <math>\langle \Delta\Theta_\nu \rangle</math>, versus different noise levels<br/>and antenna spacings, where the station spacing is set at 1.60 km and<br/>the trigger threshold is <math>3.5\sigma_{noise}</math>. . . . .</i> | 59 |

|      |   |    |
|------|---|----|
| 4.19 | <i>Resolutions of neutrino direction, <math>\langle\Delta\Theta_\nu\rangle</math>, versus different noise levels and antenna spacings, where the station spacing is set at 1.86 km and the trigger threshold is <math>3.5\sigma_{noise}</math>.</i> | 60 |
| 4.20 | <i>Resolutions of neutrino direction, <math>\langle\Delta\Theta_\nu\rangle</math>, versus different noise levels and antenna spacings, where the station spacing is set at 1.33 km and the trigger threshold is <math>5\sigma_{noise}</math>.</i>   | 60 |
| 4.21 | <i>Resolutions of neutrino direction, <math>\langle\Delta\Theta_\nu\rangle</math>, versus different noise levels and antenna spacings, where the station spacing is set at 1.60 km and the trigger threshold is <math>5\sigma_{noise}</math>.</i>   | 61 |
| 4.22 | <i>Resolutions of neutrino direction, <math>\langle\Delta\Theta_\nu\rangle</math>, versus different noise levels and antenna spacings, where the station spacing is set at 1.86 km and the trigger threshold is <math>5\sigma_{noise}</math>.</i>   | 61 |
| 4.23 | <i>Resolutions of neutrino direction, <math>\langle\Delta\Theta_\nu\rangle</math>, versus different noise levels and antenna spacings, where the station spacing is set at 1.33 km and the trigger threshold is <math>7\sigma_{noise}</math>.</i>   | 62 |
| 4.24 | <i>Resolutions of neutrino direction, <math>\langle\Delta\Theta_\nu\rangle</math>, versus different noise levels and antenna spacings, where the station spacing is set at 1.60 km and the trigger threshold is <math>7\sigma_{noise}</math>.</i>   | 62 |
| 4.25 | <i>Resolutions of neutrino direction, <math>\langle\Delta\Theta_\nu\rangle</math>, versus different noise levels and antenna spacings, where the station spacing is set at 1.86 km and the trigger threshold is <math>7\sigma_{noise}</math>.</i>   | 63 |



|      |  |    |
|------|--|----|
| 4.26 | <i>Detection Efficiencies versus different noise levels and antenna spacings, with the station spacing of 1.33 km and the trigger threshold is <math>3.5\sigma_{noise}</math>.</i> | 63 |
| 4.27 | <i>Detection Efficiencies versus different noise levels and antenna spacings, with station spacing as 1.60 km and the trigger threshold is <math>3.5\sigma_{noise}</math>.</i>     | 64 |
| 4.28 | <i>Detection Efficiencies versus different noise levels and antenna spacings, with station spacing as 1.86 km and the trigger threshold is <math>3.5\sigma_{noise}</math>.</i>     | 64 |
| 4.29 | <i>Detection Efficiencies versus different noise levels and antenna spacings, with the station spacing of 1.33 km and the trigger threshold is <math>5\sigma_{noise}</math>.</i>   | 65 |
| 4.30 | <i>Detection Efficiencies versus different noise levels and antenna spacings, with station spacing as 1.60 km and the trigger threshold is <math>5\sigma_{noise}</math>.</i>       | 65 |
| 4.31 | <i>Detection Efficiencies versus different noise levels and antenna spacings, with station spacing as 1.86 km and the trigger threshold is <math>5\sigma_{noise}</math>.</i>       | 66 |
| 4.32 | <i>Detection Efficiencies versus different noise levels and antenna spacings, with the station spacing of 1.33 km and the trigger threshold is <math>7\sigma_{noise}</math>.</i>   | 66 |
| 4.33 | <i>Detection Efficiencies versus different noise levels and antenna spacings, with station spacing as 1.60 km and the trigger threshold is <math>7\sigma_{noise}</math>.</i>       | 67 |



4.34 *Detection Efficiencies versus different noise levels and antenna spacings, with station spacing as 1.86 km and the trigger threshold is  $7\sigma_{noise}$ .* 67


5.1 *Resolution of neutrino moving direction in  $\theta$  direction in the simulation for ARIANNA.* . . . . . 69



# Chapter 1

## Introduction

### 1.1 The Mystery of Cosmic Accelerators



There are many energetic particles coming from outer space to Earth, mainly protons, heavier nuclei, or electrons. These are named cosmic rays (CRs). The energy of cosmic rays has a wide range. Scientists have been trying to explain where these particles come from, and how the sources accelerate them. Figure 1.1 shows the CR energy spectrum, including protons, antiprotons, electrons, and positrons. Each data point is the differential flux,  $dN/dE$ , multiplied by  $E^2$  [1]. This spectrum steepens around  $3 \times 10^{15}$  eV (where people call it the "knee") and flattens around  $3 \times 10^{18}$  eV (where people call it the "ankle"). Scientists have tried to explain how these two features form.

It is believed that most cosmic rays originate from extrasolar sources within our own galaxy such as rotating neutron stars, supernovae, and black holes. However, the fact that some cosmic rays have extremely high energies provides evidence that

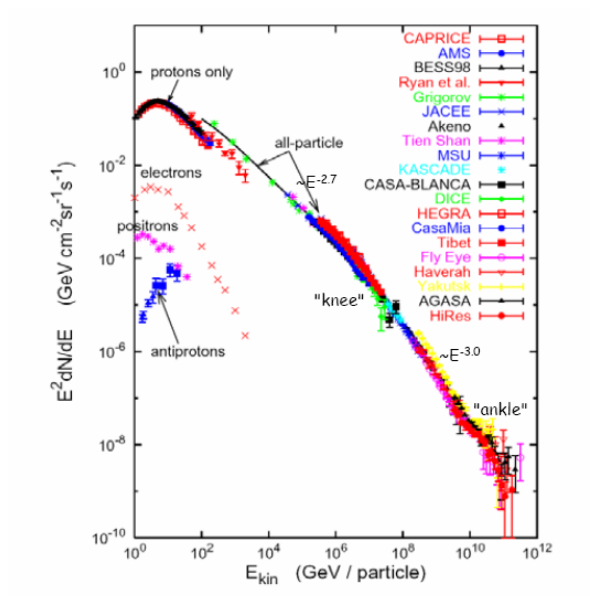


Figure 1.1: *This is a CR energy spectrum of  $E^2 dN/dE$  for protons, antiprotons, electrons, and positrons.*

at least some must be of extra-galactic origin (e.g. radio galaxies and quasars); the local galactic magnetic field would not be able to contain particles with such a high energy. The origin of cosmic rays with energies up to 10<sup>14</sup> eV can be accounted for in terms of shock-wave acceleration in supernova shells.

Observations have shown that cosmic rays with an energy above 10 GeV approach the Earth's surface isotropically; it has been hypothesized that this is not due to an even distribution of cosmic ray sources, but instead is due to galactic magnetic fields causing cosmic rays to travel in spiral paths. This limits cosmic ray's usefulness in positional astronomy as they carry no information of their direction of origin. At energies below 10 GeV there is a directional dependence, due to the interaction of the charged component of the cosmic rays with the Earth's magnetic field.

The shapes of cosmic ray trajectories in the Galaxy result from the effect of the chaotic and regular magnetic field, the rates of the nuclear collisions, the gas density and other minor parameters. For a given magnetic field configuration the forms of the trajectories, regardless of their lengths, can be either in rectilinear or tortuous, depending on the ion energy [2]. It is shown that the ankle and the knee energies of individual ions correspond to those particular energies of the ion traversing the Milky Way which mark, respectively, the rectilinear and tortuous propagation.

The origin of cosmic rays with energy greater than  $10^{14}$  eV remains unknown. Since the first detection of cosmic rays with the highest energy of that time ( $10^{20}$ eV) by Yakutsk air shower array in 1989 [3], the question of what astrophysical object or process can produce such high energy particles has been puzzling scientists. There are many models proposed, such as the traditional bottom-up astrophysical acceleration models [4], including active galactic nuclei (AGN), gamma ray bursts (GRB), and etc., as the sources, or the exotic top-down particle physics models [5], including annihilation of dark matter, super heavy dark matter particles decay, topological defects, and etc. However, neither of these models can easily explain how some of the cosmic rays can get such high energy. On the other hand, the observations of ultra high energy cosmic rays (UHECRs, CR with energy above  $10^{19}$  eV) neither identify the source well nor uniquely determine the extragalactic source distribution, i.e. the evolution of the source co-moving density, or the source spectrum [6]. As a result, what our cosmic accelerators are remains mysterious.

## 1.2 Greisen-Zatsepin-Kuzmin(GZK) Cutoff and GZK

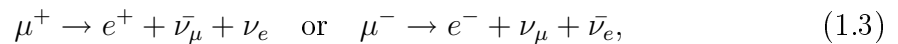
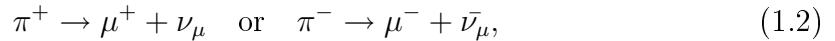
### Process

A limit on the cosmic ray energy was suggested in 1966 by Kenneth Greisen (US) [7] and Vadim Kuzmin and Georgiy Zatsepin (Russia) [8] independently based on interactions between the cosmic ray and the photons of the cosmic microwave background radiation. They predicted that cosmic rays with energies over the threshold energy of  $6 \times 10^{19}$  eV would interact with cosmic microwave background photons to produce pions. This would continue until their energies fall below the pion production threshold:



This theoretical upper limit on the energy of cosmic rays from distant sources will create a cutoff in the cosmic ray spectrum right at the energy level of  $6 \times 10^{19}$  eV. And thus we call this GZK limit or GZK cutoff.

Furthermore, the interaction of photons and protons does not stop at pion productions. These pions continue to decay into neutrinos:





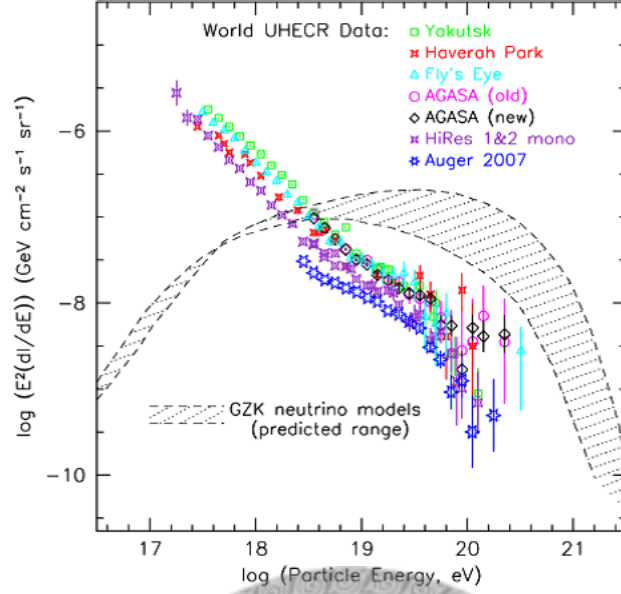


Figure 1.2: *Energy spectrum of UHECR observation and GZK neutrino prediction.*

The whole interaction, including Eqs. 1.1 to 1.4, is named as GZK process, and the neutrinos produced from GZK process are called GZK neutrinos. The energy of GZK neutrino is also very high, still above the level of  $10^{19}$  eV, so it can deserve the name of UHE neutrino. Figure 1.2 shows the energy spectrum of UHECR observation and GZK neutrino prediction. The GZK neutrino models in this figure were proposed by Kalashev [11], Protheroe, and Johnson [12] et al., and UHECR observation data are taken from Auger [13], Yakutsk [14], the Fly's Eye [15], AGASA [16], HiRes [17], and Haverah Park [18]. Error bars here only include statistical errors.

Because of the mean free path associated with the interaction, extragalactic cosmic rays with distances more than 50 Mpc (163 Mly) from the Earth with energies greater than this threshold energy should never be observable on Earth, i.e., a hori-

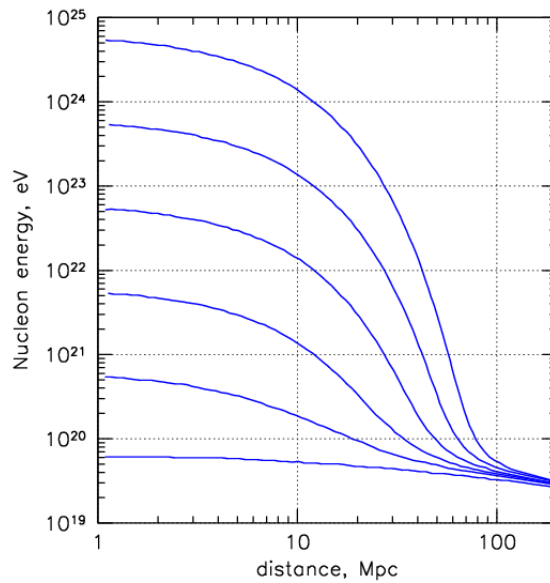


Figure 1.3: *Nucleon energy vs. traveling distance.*

zon of UHECRs is formed and there are no known sources within this distance that could produce them. From Fig. 1.3, we can see that the proton energy above  $6 \times 10^{19}$  eV will lose its energy while traveling through the universe, due to the GZK process [19].

### 1.3 UHE Neutrino: Key to the Mystery of Cosmic Accelerators

To find out a proper approach to probe the nature of the cosmic accelerators, it is beneficial to consider each kind of astrophysical messengers available to us. For the charged messengers, protons take a dominating ratio of the cosmic rays. However, they cannot point back to the source well because they would be deflected by the

magnetic field. As to the charged-neutral messengers, photons have the greatest quantity, but unfortunately they lose energy through pair production on IR and 3K microwave background when they have energies above 30 TeV. We can see the range and energy limitation of photons or protons as messengers in Fig. 1.4 [20].

Luckily, a third option, GZK neutrinos, can be useful messengers because they are the by-product from the interaction of protons or other heavier nuclei with CMB photons. And most important of all, they are not deflected by the magnetic field and do not lose energy after going through CMB photons. In other words, this kind of neutrinos can keep their high energy and thus we can identify them from UHECRs and even use them to point back to the vertex where they were produced. Furthermore, since UHECRs very likely undergo this kind of interaction after they travel through CMB photons for distance of one energy loss length, this vertex will look angularly very close to the source of UHECRs as long as this vertex or this source is very distant to the observer. The angle between the line of sight of this source and the neutrino incoming direction is called the deviation angle of the GZK neutrino. An assessment will be given in Chapter 2 to describe how small this deviation angle is, in order to see the probability of utilizing cosmogenic neutrinos to point back to the UHECR sources, the cosmic accelerators.

## 1.4 Detection of UHE neutrinos

Since UHE neutrinos can be a proof of the GZK process, but also a key to unveil the mystery of the cosmic accelerator, detection of them is scientifically important. Neu-

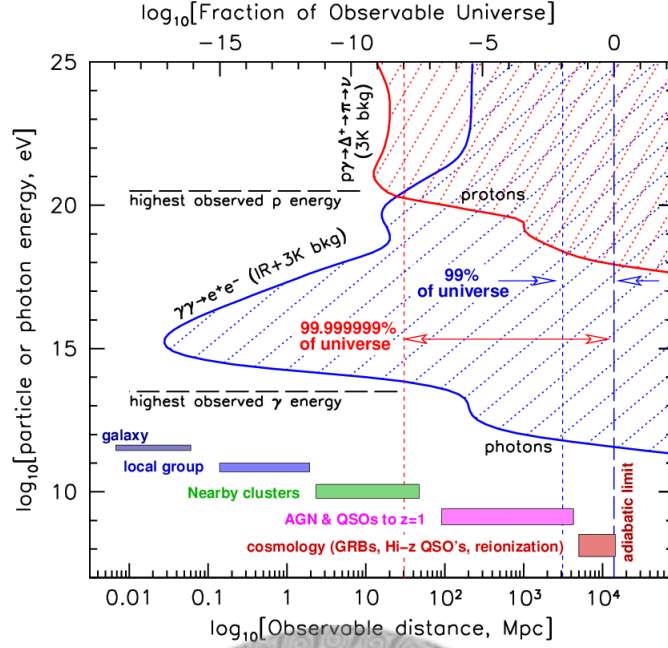


Figure 1.4: *Range and energy limitation of photons or protons as astrophysical messengers.*

trinos cannot be directly observed, they but can be indirectly observed through their interactions with ordinary matter. There are three possible neutrino interactions. These are the elastic scattering:

$$\nu_e + e^- \rightarrow \nu_e + e^-, \quad (1.5)$$

the charge current (CC) interaction:

$$\nu_l + N \rightarrow l^- + X \quad \text{or} \quad \bar{\nu}_l + N \rightarrow l^+ + X, \quad (1.6)$$

and the neutral current (NC) interaction:

$$\nu_l + N \rightarrow \nu_l + X \quad \text{or} \quad \bar{\nu}_l + N \rightarrow \bar{\nu}_l + X, \quad (1.7)$$

where  $l^\pm$  can be  $e^\pm$ ,  $\mu^\pm$ , or  $\tau^\pm$ ;  $N$  stands for a nucleus, and  $X$  is a nucleus in its excited state. The outgoing  $\mu^\pm$  or  $\tau^\pm$  would emit Cherenkov radiation and also have

chance to cause an electromagnetic (EM) shower through Bremsstrahlung and pair production, or a hadronic shower through photonuclear interaction. As for  $e^\pm$ , they would result in EM showers transiently because of their large cross sections with matter. On the other hand,  $X$  would cause a hadronic shower.

The EM shower is less favorable for observation because the LPM effect would reduce the cross sections of Bremsstrahlung and pair production at high energies or in high matter densities. In contrast, a hadronic shower would, due to Askaryan effect [21], result in 20% excess of fast moving negative charges and produce Cherenkov radiation, the radio band of which is coherent in ice and can be employed as the probe for UHE neutrinos.

Askaryan Effect is named after Gurgun Askaryan, a Soviet-Armenian physicist who postulated it in 1962. It states that a high energy particle which travel faster than light in dense dielectric material can lead to charge asymmetry because of high energy interactions such as Compton, Bhabha, and Moller scattering, along with positron annihilation in the electron-photon part of a particle cascade. Then these fast moving charges cause Cherenkov radiation, the radio and microwave bands of which are coherent. By Askaryan effect, UHE neutrinos could be observed, so the Antarctic Impulse Transient Antenna (ANITA) collaboration, which intends to detect cosmogenic neutrinos with the ice in the Antarctic, performed an experiment at the Stanford Linear Accelerator Center (SLAC) in June 2006, and confirmed this effect in ice [22]. The relation between the field strength and the frequency in radio band, and the radiative Cherenkov power depending on the shower energy are shown

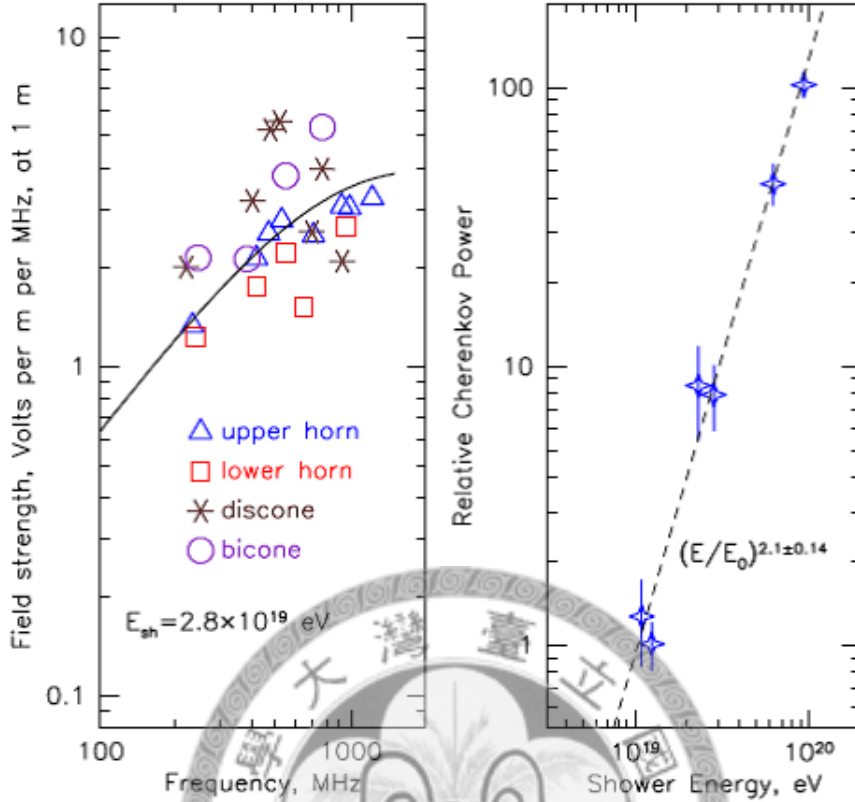


Figure 1.5: *Askaryan effect in ice: field strength vs frequency in radio band and radiative Cherenkov power vs. shower energy.*

in Fig. 1.5. The angular dependence of the Cherenkov field strength is shown in Fig. 1.6.

## 1.5 Radio Detection Experiments of UHE Neutrino: ARA Design Concepts

Askaryan Radio Array (ARA) is a large-scale radio Cherenkov detector which scientists propose to develop in Antarctica [23, 24], aiming for discovering the origin and

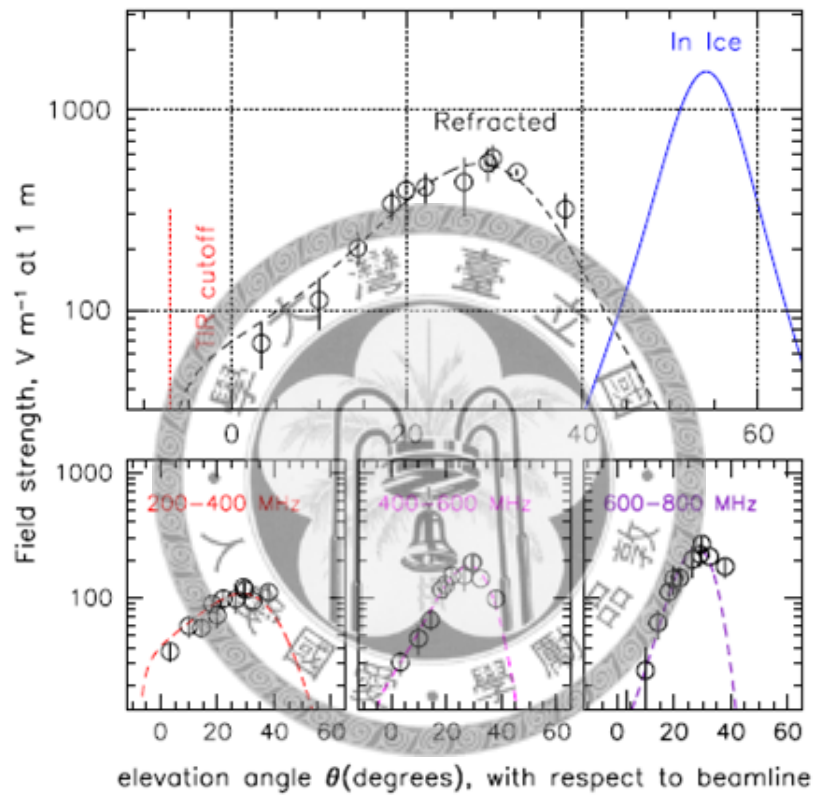


Figure 1.6: Askaryan effect in ice: angular dependence of Cherenkov field strength.

evolution of the cosmic accelerators that produce the highest energy cosmic ray, by means of observing the ultra high energy (UHE) cosmogenic neutrinos.

The reasons why ARA choose the Antarctic as the experiment site are following:

1. There is plenty of ice as the target for detecting neutrinos.
2. The ice is so transparent to the RF shower signal that the spacing of RF detectors can be sufficiently large to enhance the effective volume and event rate.
3. It is more radio-quiet than other places in the world so as to reduce artificial signals considerably.
4. The temperature is so low that the background noise also reduces considerably.

Therefore, antarctic is a very proper site to do the UHE neutrino experiment. With such a nature given experimental environment, the next issue would be how to optimize the array geometry so as to maximize the performance.

The primary goal of this thesis work is to assess and optimize the capability of ARA, particularly the capability of reconstructing neutrino incoming directions, by means of Monte Carlo simulations. In the following parts of this thesis, the simulation method will be described in Chapter 3, and results will be presented in Chapter 4, with a summary given in the end. Note that Chapter 2 is the assessment of the deviation angle of the cosmogenic neutrino, and the motivation of this study can be found in Section 1.3.



# Chapter 2

## Deviation Angle of Cosmogenic

## Neutrino

### 2.1 A New Quantity to Measure the Deviation: $\theta_{max}$

Due to their small cross-section, GZK neutrinos propagate through the universe with hardly any interaction, and hence it is possible to utilize these neutrinos to trace back to the cosmic accelerators. However, the neutrino tracks do not necessarily point back precisely to the accelerator. Because their parent particles are charged particles, which might be ejected from the accelerator and could be deflected by the magnetic field in the vicinity of the accelerator and then produce these neutrinos through the GZK process, there might be an angular separation between the neutrino directions and their parent particle directions at the source, i.e. before neutrinos are produced and begin to travel in straight lines, there already exists deviation angles from them. Fortunately, most of these GZK neutrinos are produced within the GZK

sphere, i.e. the radius within which the original UHE proton would lose most of its energy, which is roughly 50 Mpc. In the following analysis, we take the energy loss length,  $L_{loss}$ , as this radius.

As shown in Fig. 2.1, an AGN is taken as an example of the cosmic accelerator, and protons as an example of charged nuclei. Most GZK neutrinos are produced within a sphere of radius of  $L_{loss}$ , centered at the AGN. The deviation angle of a GZK neutrino reaches maximum when this neutrino is produced on the surface of the sphere. For an AGN, it has a fixed angular diameter distance  $D_A$ . For a certain energy level of a proton, it has a fixed energy loss length  $L_{loss}$ . Thus, keeping these two variables fixed, the maximum deviation angle,  $\theta_{max}$  can be determined. If one, by employing cosmological knowledge, converts  $D_A$  to redshift,  $z$ , then  $\theta_{max}$  as a function of  $z$  and  $L_{loss}$  can be obtained.

Furthermore, for a certain level of GZK neutrino energy, if its flux as a function of the redshift is given, then one also knows the probability on the Earth to receive a GZK neutrino from a certain range of  $z$ . The probability of receiving a GZK neutrino within a certain range of  $\theta_{max}$  can be readily acquired according to the relation of  $z$  and  $\theta_{max}$ . From this, one expects that the observed GZK neutrino would be deviated at most for a certain angle, given a certain level of confidence. This is the upper bound of the deviation angle of GZK neutrinos with respect to the center of the AGN.

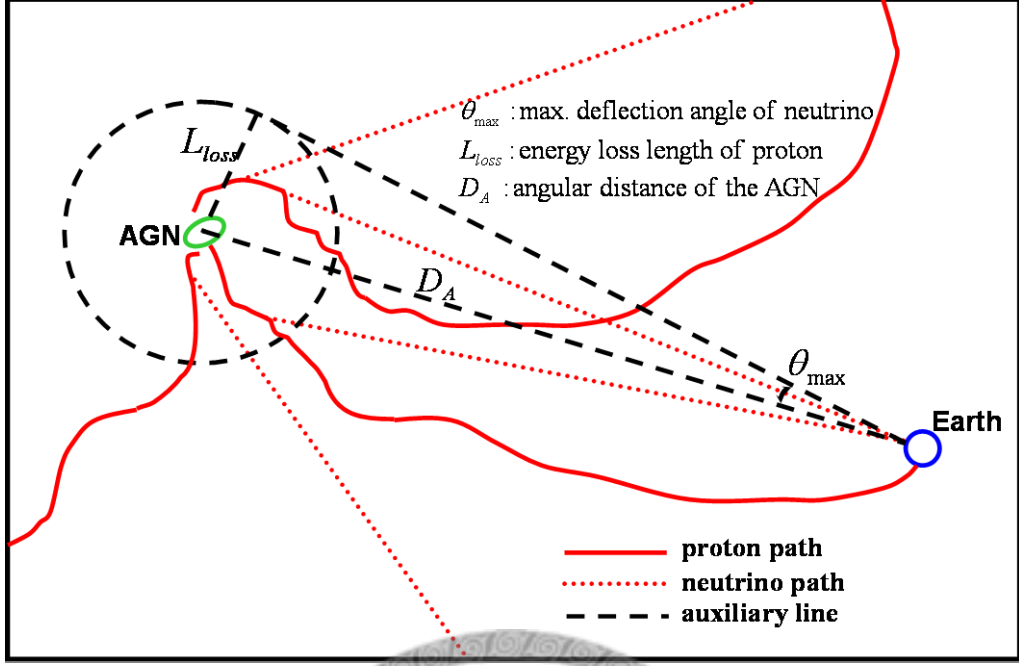
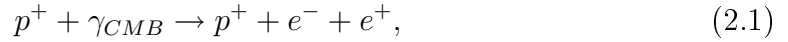


Figure 2.1: *Illustration of how protons and GZK neutrinos travel from AGN to the Earth.*

## 2.2 Proton Energy Loss Length

For the propagation of protons above  $\text{EeV}(10^{18})$  energy level, there are two dominant energy loss processes in addition to the adiabatic energy loss. These are the pair production,



and the pion production (Eq.1.1 and 1.2). However, above the energy threshold of GZK process ( $>10^{20}\text{eV}$ ), only pion production dominates [25], and the analysis in this work is also done in this pion-production-dominating domain.

The proton energy loss length is defined as [26]

$$L_{loss} \equiv \left( \frac{1}{E} \frac{dE}{dx} \right)^{-1}, \quad (2.2)$$

$$R \equiv \frac{K_p dE}{E dx}. \quad (2.3)$$

$R$  is the attenuation rate and  $K_p$  the inelasticity of proton for  $p\gamma$  interaction, which can be obtained as follows [25]:

$$R = \frac{1}{2\Gamma_p^2} \int_0^\infty \frac{1}{\varepsilon_\gamma^2} \frac{dn_\gamma}{d\varepsilon_\gamma} d\varepsilon_\gamma \int_0^{2\Gamma_p \varepsilon_\gamma} \varepsilon'_\gamma \sigma_{p\gamma}(\varepsilon'_\gamma) K_p d\varepsilon'_\gamma, \quad (2.4)$$

$$K_p = \Delta E_p / E_p, \quad (2.5)$$

$$\Gamma_p = E_p / m_p, \quad (2.6)$$

where  $m_p$  is the proton mass,  $\varepsilon_\gamma$  photon energy, and  $\sigma_{p\gamma}$  the cross section of  $p\gamma$  interaction. The inelasticity can be approximated as follows, with low pion multiplicities [27]:

$$K_p \approx \frac{m_\pi^2 + 2m_p \varepsilon'_\gamma}{2(m_p^2 + 2m_p \varepsilon'_\gamma)}. \quad (2.7)$$

To make further approximation, a top-hat function is used to describe the cross section above [28],

$$\begin{aligned} \sigma_{p\gamma}(\varepsilon'_\gamma) &= 0 \text{ if } \varepsilon'_\Delta + \delta \leq \varepsilon'_\gamma \\ &= \sigma_\Delta \text{ if } \varepsilon'_\Delta - \delta \leq \varepsilon'_\gamma \leq \varepsilon'_\Delta + \delta \\ &= 0 \text{ if } \varepsilon'_\gamma \leq \varepsilon'_\Delta - \delta. \end{aligned} \quad (2.8)$$

Here, the peak value of the cross section, at  $\Delta$  resonance, is  $\sigma_\Delta \sim 0.5$  mb. And  $\varepsilon'_\Delta \sim 340$  MeV,  $\delta \sim \text{MeV}$ , and  $K_p \sim 0.2$  when this interaction occurs nearby the threshold. Then, one obtains the attenuation rate in the following form:

$$R(E_p) \sim 0.2 \sigma_{p\gamma} \int_0^\infty \frac{1}{E^2} \frac{dn_\gamma}{d\varepsilon_\gamma} d\varepsilon_\gamma \approx 0.2 \left[ \frac{l_0 e^x}{1 - e^{-x}} \right]^{-1}, \quad (2.9)$$

where  $l_0 = 5$  Mpc, and  $x = 10^{20.53} \text{eV}/E_p$ .

In the GZK process, the proton-neutrino energy relation is [25]:

$$E_\nu \sim 0.05E_p, \quad (2.10)$$

for the case of the pion decay which are followed by the muon decay, or

$$E_\nu \sim 0.000E_p, \quad (2.11)$$

for the case of the neutron decay.

In this chapter, we'll calculate the upper bound of the GZK neutrino deviation angle at the energy level of  $10^{19}$  eV. Therefore, the proton energies can be roughly  $2 \times 10^{20}$  eV or  $2 \times 10^{22}$  eV, which correspond to two proton energy loss lengths. The longer energy loss length, i.e. the one associated with  $2 \times 10^{20}$  eV, will be taken because we intend to calculate the upper bound of the neutrino deviation angle.

Due to the expansion of the universe, the CMB photons have higher number density and higher energy at the earlier epoch and thus the proton energy loss length varies with the redshift,  $z$ . The scaling relation has the following form [29]:

$$L_{loss}(E, z) = (1 + z)^{-3} L_{loss}[(1 + z)E, 0], \quad (2.12)$$

where the  $(1 + z)^{-3}$  factor can be attributed to the density increase of the CMB photons, and the  $(1 + z)$  factor in  $L_{loss}[(1 + z)E, 0]$  can be attributed to the energy increase of the CMB photons. Figure 2.2 shows the proton energy loss length,  $L_{loss}$ , as a function of  $z + 1$ , where the proton energy is set as  $2 \times 10^{20}$  eV. This figure results from Eq. 2.9 and 2.12.

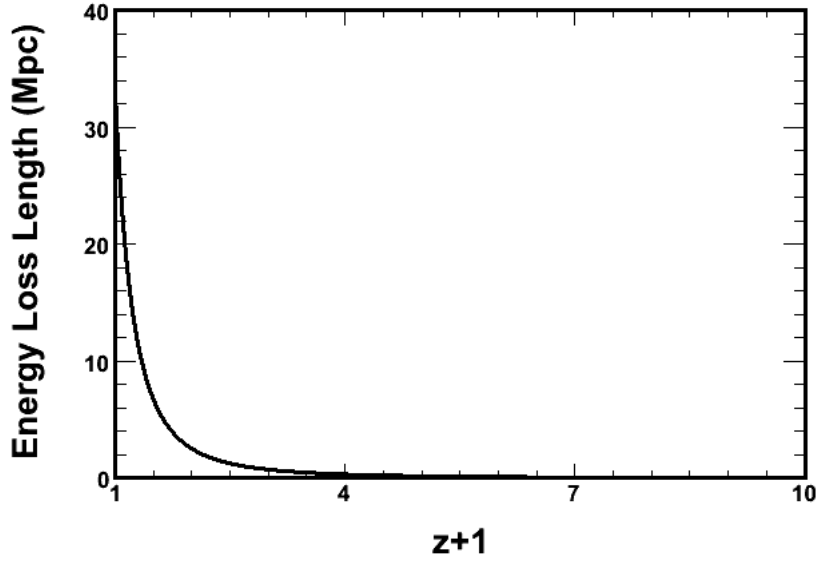


Figure 2.2: Proton energy loss length,  $L_{loss}$  as a function of  $z + 1$ , where the proton energy is set as  $2 \times 10^{20} eV$ , where  $z$  is the redshift.

### 2.3 Angular Diameter Distance

Angular diameter distance of an astrophysical object is defined by its transverse physical size and angular size:

$$D_A \cdot \theta \approx l_{size}. \quad (2.13)$$

In this analysis, the distance of UHECR source is the angular diameter distance. Its transverse physical size is the diameter of the sphere with  $L_{loss}$  as its radius, and its angular size is twice as large as the neutrino deviation angle.

The angular diameter distance can be described by the redshift of that astrophysical object,  $z$ :

$$D_A = \frac{1}{1+z} \int \frac{c}{H} dz, \quad (2.14)$$

$$H = H_0 [\Omega_M(0)(1+z)^3 + \Omega_\gamma(0)(1+z)^4 + \Omega_V(0) + \Omega_K(0)(1+z)^2]^{1/2}, \quad (2.15)$$

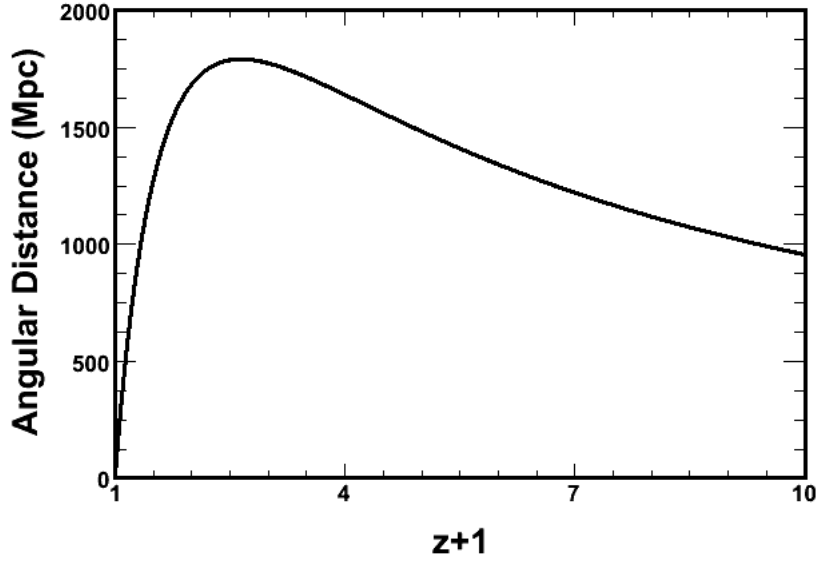


Figure 2.3: Angular diameter distance as a function of  $z + 1$ .

where the Hubble constant  $H_0$  is  $70 \text{ km s}^{-1} \text{ Mpc}^{-1}$ , density parameter of matter  $\Omega_M = 0.27$ , density parameter of cosmological constant  $\Omega_\Lambda = 0.73$ , density parameter of radiation  $\Omega_R = 8.57 \times 10^{-5}$ , and density parameter of the curvature  $\Omega_K = 1 - \Omega_M - \Omega_R - \Omega_\Lambda$ . Figure 2.3 shows angular diameter distance in units of Mpc as a function of  $z + 1$ . This results directly from Eq. 2.14. Since the explicit forms of the angular diameter distance,  $D_A(z)$ , and the proton energy loss length,  $L_{loss}(z)$ , are obtained, the maximum deviation angle of the neutrino,  $\theta_{max}$ , as a function of  $z$  can be easily derived:

$$\theta_{max} = \sin^{-1}\left(\frac{L_{loss}}{D_A}\right). \quad (2.16)$$

Figure 2.4 shows the maximum deviation angle of neutrino,  $\theta_{max}$ , in unit of degree, as a function of  $z + 1$ .

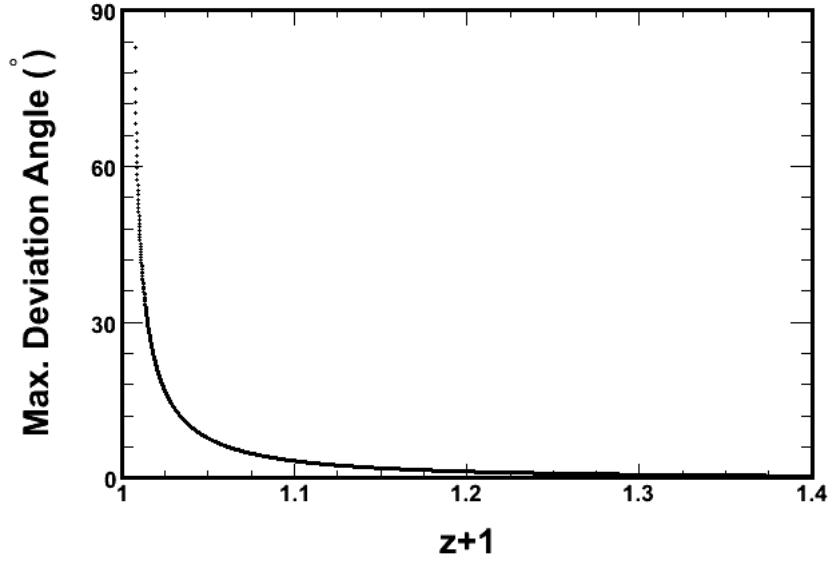


Figure 2.4: Maximum deviation angle of a GZK neutrino,  $\theta_{max}$ , as a function of  $z + 1$ .

## 2.4 GZK Neutrino Flux from Proton Propagation

For a certain energy level of GZK neutrinos, its flux as a function of the redshift can be obtained from the integration of the source distribution function,  $L$ , and neutrino yield function,  $Y$ . To simplify the problem, a homogeneous source distribution with identical proton injection spectra is employed. The local GZK neutrino flux per redshift with flavor  $i$  and energy  $E_\nu$  is [30]:

$$\frac{dF_i(E_{\nu_i})}{dz} = \frac{c}{4\pi E_{\nu_i}} \int L(z, E_p^s) Y(E_p^s, E_{\nu_i}, z) \frac{dE_p^s}{E_p^s}. \quad (2.17)$$

The neutrino yield function is described as

$$Y(E_p^s, E_{\nu_i}, z) = E_{\nu_i} \frac{dN_{\nu_i}}{dE_{\nu_i}}, \quad (2.18)$$



which is evaluated with Monte Carlo for a 200 Mpc source using SOPHIA [31]. The scaling relation is

$$Y(E_p^s, E_{\nu_i}, z) = Y((1+z)E_p^s, (1+z)^2 E_{\nu_i}, 0), \quad (2.19)$$

and the source function per unit redshift is

$$L(z, E_p^s) = H(z)\eta(z)L_0E_p^s. \quad (2.20)$$

The cosmological evolution of cosmic ray sources :

$$\begin{aligned} H(z) &= (1+z)^3 \text{ if } z \leq 1.9, \\ &= (1+1.9)^3 \text{ if } 1.9 \leq z \leq 2.7, \\ &= (1+1.9)^3 e^{(2.7-z)/2.7} \text{ if } 2.7 \leq z. \end{aligned} \quad (2.21)$$

The metric element for Einstein-de Sitter universe is defined as

$$\eta(z) = \frac{dt}{dz} = \frac{1}{H_0(1+z)^{5/2}}, \quad (2.22)$$

and the source proton function per unit redshift [32] is given as

$$L_0(E_p^s) = (4.5 \times 10^{44} \text{ erg/Mpc/yr}) \left( \int_{10^{19}}^{10^{21}} E_p^s \frac{dN_p}{dE_p^s} dE_p^s \right)^{-1} dE_p^s \frac{dN_p}{dE_p^s}. \quad (2.23)$$

$$\frac{dN_p}{dE_p^s} \propto E_p^{s-2} e^{-E_p^s/10^{21.5} \text{ eV}}. \quad (2.24)$$

Figure 2.5 illustrates the local GZK neutrino flux per  $(z+1)$  at the energy of  $10^{19}$  eV.

Since the maximum deviation angle of GZK neutrino is determined for a specific cosmological epoch, and the GZK neutrino flux from this epoch is also obtained from a homogeneous UHECR source model, one can acquire the neutrino flux histogram with respect to its maximum deviation angle. Figure 2.6 shows the GZK neutrino

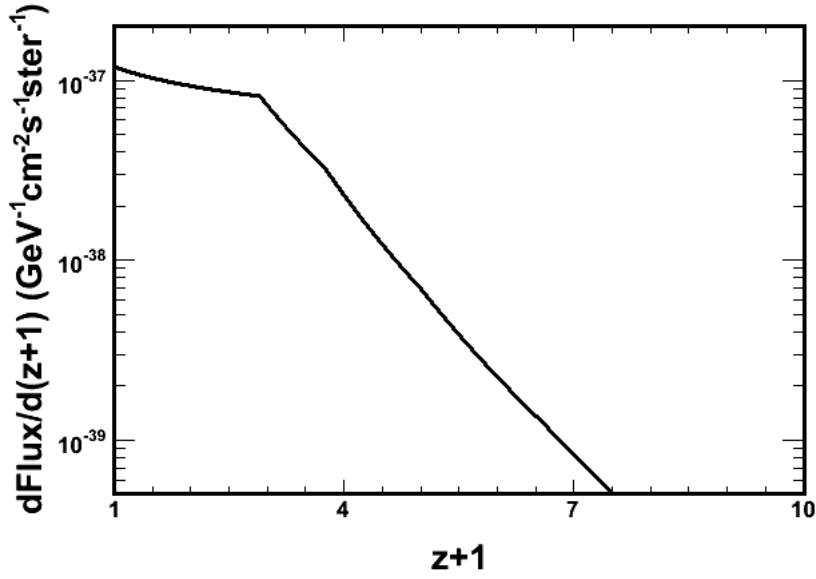


Figure 2.5: *The local GZK neutrino flux per (z+1) at the energy of  $10^{19}$  eV*

flux histogram (in unit of per  $\text{cm}^2\text{-s-ster}$ ) with respect to its maximum deviation angle (in unit of degree). This figure implies the relative probability with which the observed neutrinos of  $10^{19}\text{eV}$  have been deviated. As can be seen from this figure, the neutrinos which had been deviated by at most 2 degrees have the largest flux or the highest probability. The full width at half maximum (FWHM) of the maximum deviation angle is 0.031 degree.

## 2.5 Conclusion of the Assessment

To quantitatively describe the confidence level with which the observed neutrinos had been deviated within a certain angle, one can use the accumulative probability of observing neutrinos under the maximum deviation angle ranging from zero to a certain angle. The result is in Fig. 2.7. It shows that, at the confidence level of 90%,

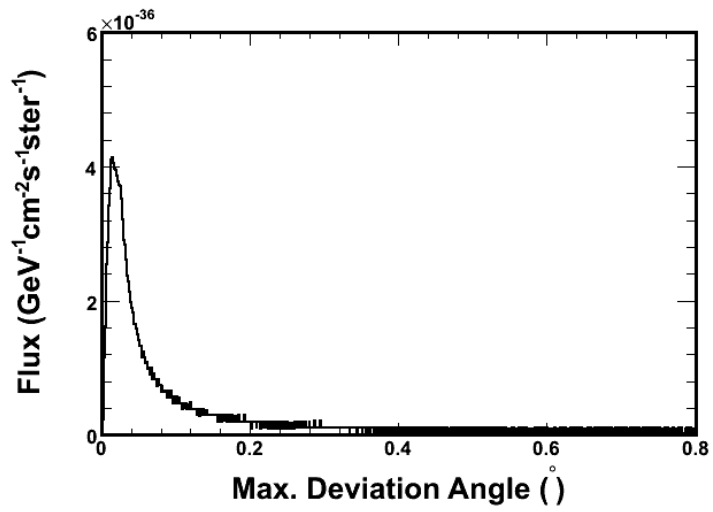


Figure 2.6: *GZK neutrino flux as a function of its maximum deviation angle.*

one observes neutrinos to deviate within one degree, i.e.,  $\theta_{max} = 1^\circ$  (90% confidence level).



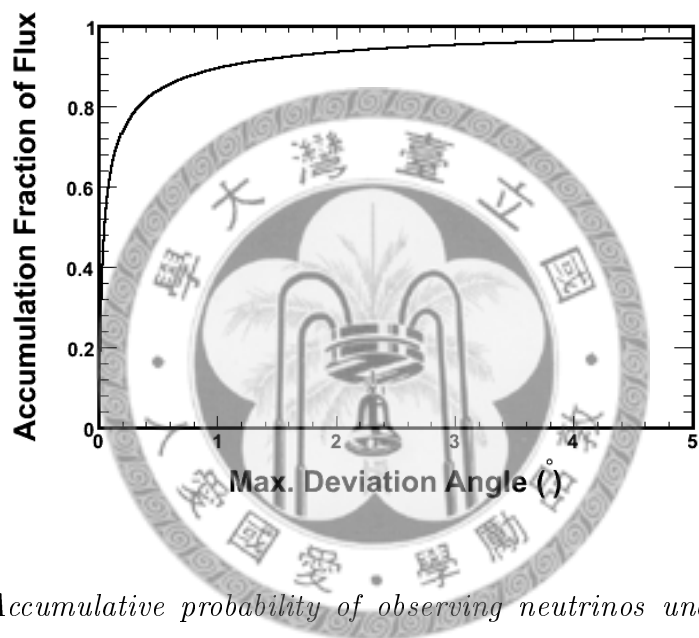
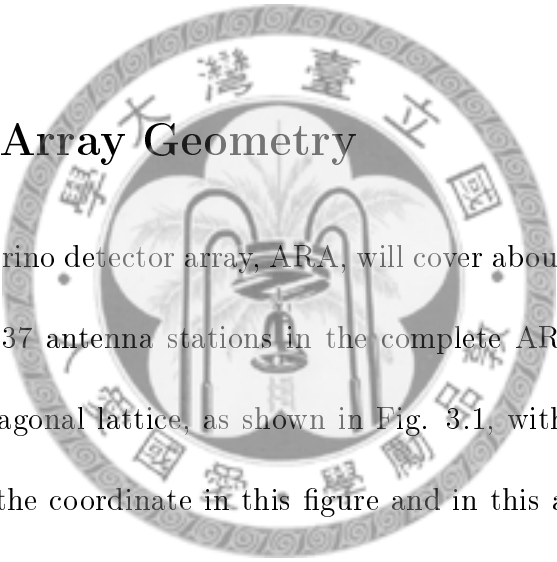


Figure 2.7: *Accumulative probability of observing neutrinos under the maximum deviation angle ranging from zero to a certain angle.*

# Chapter 3

## Simulation Method

### 3.1 Setting Array Geometry



The radio-based neutrino detector array, ARA, will cover about 80 km<sup>2</sup> at the South Pole. There will be 37 antenna stations in the complete ARA. These 37 stations are located on a hexagonal lattice, as shown in Fig. 3.1, with a station spacing of 1.33 km. Note that the coordinate in this figure and in this analysis has its origin defined at the center of ARA, on the surface of the ice, and the z axis points to the sky.

Each station is composed of a triad of boreholes with depths of 200 m, on the corners of an equilateral triangle. Each borehole has four antennas, two of which are the horizontal-polarization (Hpol) antennas and the other two the vertical-polarization (Vpol) antennas, as shown in Fig. 3.2. A pair of antennas, a Hpol one and a Vpol one, can detect the strengths of electrical field projected to horizontal plane (2D) and vertical line (1D) respectively, and the find the possible direction of the elec-

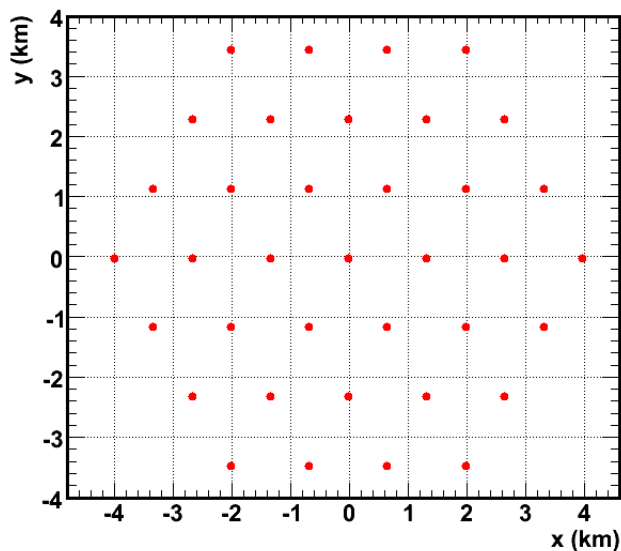


Figure 3.1: *The geometry of the distribution and their coordinates.*

tric field. The side length of the equilateral triangle and the distance between two Vpol antennas in a borehole, are set the same, at 30 m. The location coordinate of antenna  $i$  is denoted as  $x_i^{ant}$ .

## 3.2 Event Production

In the simulation, the shower events resulted from the CC or NC interactions are generated in the ice. This event generation does not differentiate neutrinos or anti-neutrinos, and flavors are not considered, either. In each event, 6 parameters are generated, including the shower location,  $x_{sh}^{gen}, y_{sh}^{gen}, z_{sh}^{gen}$ , the moving direction of neutrino:  $\theta_\nu^{gen}, \phi_\nu^{gen}$ , and the intensity of the radio Cherenkov radiation induced by the shower followed by this interaction,  $V_0^{gen}$ . We treat the shower location the

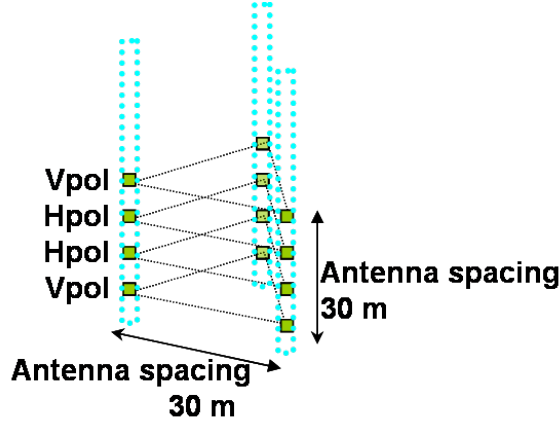


Figure 3.2: *ARA antenna cluster geometry in a station, where there are twelve antennas, indicated by green squares.*

same as the neutrino interaction vertex because of the small shower size in ice. The generated shower locations are uniformly distributed over a cylinder volume, where the center of the cylinder volume is located at the center of ARA. This volume has an axis along the vertical direction passing through the center of ARA, and has a radius of 6 km and a height from  $z = -2$  km to  $z = 0$ . Therefore, we have

$$0 < \sqrt{x_{sh}^{gen2} + y_{sh}^{gen2}} < 6\text{km}, \quad (3.1)$$

$$-2\text{km} < z_{sh}^{gen} < 0. \quad (3.2)$$

The reason why we set the height of this event cylinder as 2 km is that the thickness of the ice in Antarctic is approximately 2 km. The choice of 6 km for the radius is due to the following reason. For the events with shower locations far away from ARA detectors, its radio radiation can not reach ARA because of attenuation. Therefore, the farthest distance for the radio signal of the event to travel to the ARA center is approximately estimated as  $1\text{km} + 1.33\text{km} \times 3 = 5\text{km}$ . For safety reason, we set

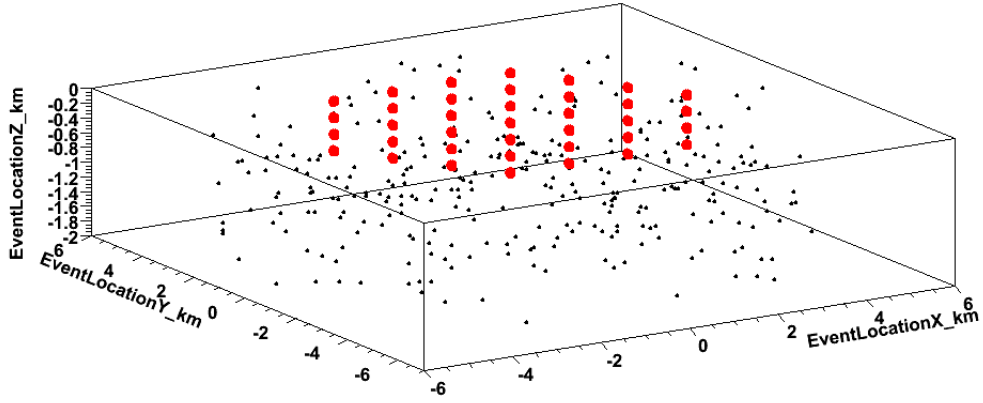


Figure 3.3: *The shower location field and the 37 ARA stations.*

it as 6 km rather than 5 km. The shower location field and the 37 ARA stations are shown in Fig. 3.3. Black dots are the generated shower locations, distributed uniformly in this field. Red circles represent the 37 stations. The moving directions of the neutrinos are also set uniformly distributed over  $4\pi$  solid angle. That is,

$$0 < \theta_{\nu}^{gen} < \pi, \quad (3.3)$$

$$0 < \phi_{\nu}^{gen} < 2\pi. \quad (3.4)$$

Furthermore, the outcome of a recorded waveform has been converted into voltage from electric field through the readout electronics and thus we set the initial intensity of the Cherenkov radiation in terms of the voltage,  $V_0^{gen}$ , as

$$0 < V_0^{gen} < 5V. \quad (3.5)$$

At this stage, we generate six parameters for each event:  $x_{sh}^{gen}$ ,  $y_{sh}^{gen}$ ,  $z_{sh}^{gen}$ ,  $\theta_{\nu}^{gen}$ ,  $\phi_{\nu}^{gen}$ ,  $V_0^{gen}$ . The first three are also denoted as the shower location vector,  $\mathbf{x}_{sh}^{gen}$ . The next



two can also be described by a unit vector,  $\mathbf{p}_\nu^{gen}$ . There are 300 simulation events generated in each simulation.

And these six event parameters are to be determined through  $\chi^2$  fit in the next few sections.

### 3.3 Radio Cherenkov Wave from the shower location to Antennas

The Cherenkov radiation is set as a point source radiation because the shower size is of the order of  $\sim\text{m}$  and the propagation length before being received is  $\sim\text{km}$ . The radiation wave front has a cone shape with the apex at the interaction location, with the axis along the neutrino moving direction, and the span angle of the RF wave from 55 degree to 57 degree. The voltage waveform of this radiation signal is set as a bipolar wave:

$$y = x \cdot e^{-x^2/2\sigma^2}, \quad (3.6)$$

where  $y$  is voltage and  $x$  stands for time. Its shape looks like Fig. 3.4.

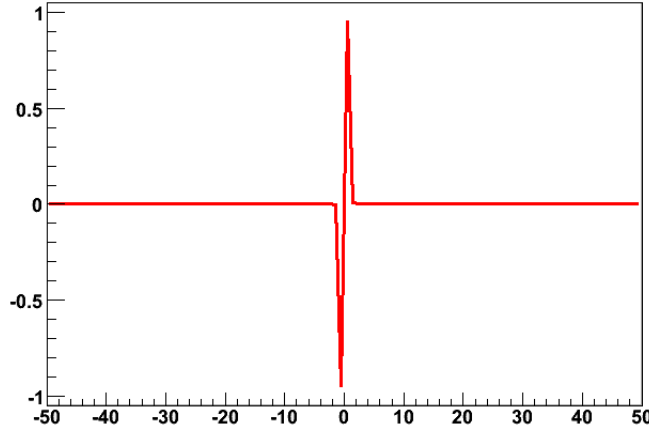


Figure 3.4: *Simulated RF waveform before reaching antennas, where the magnitude normalized to 1.*

As this wave propagates through the ice, the wave intensity attenuates as

$$\begin{aligned}
 V_i^{real}(\mathbf{x}_{sh}^{gen}, V_0, \mathbf{p}_\nu^{gen}) = & V_0^{gen} \\
 & \cdot \frac{D_0}{\sqrt{(\mathbf{x}_{sh}^{gen} - \mathbf{x}_i^{ant})^2}} \cdot e^{\sqrt{(\mathbf{x}_{sh}^{gen} - \mathbf{x}_i^{ant})^2} / L_{att}^{ice}} \\
 & \cdot a \cdot e^{-(\theta_i^{gen} - 56^\circ)^2 / 2\sigma^2} \\
 & \cdot \sin \alpha_i^{gen} \text{ for Hpol antenna } \text{ or } \cos \alpha_i^{gen} \text{ for Vpol antenna,}
 \end{aligned} \tag{3.7}$$

where  $D_0$  is the distance from the shower location to the location where  $V_0^{gen}$  is measured, 1 km,  $\theta_i^{gen}$  is the separation angle between the vector  $\mathbf{p}_\nu^{gen}$  and the vector  $\mathbf{x}_i^{ant} - \mathbf{x}_{sh}^{gen}$ , and  $\alpha_i^{gen}$  is the separation angle between the direction vector of the antenna  $i$ ,  $(x, y, z) = (0, 0, 1)$  and the direction vector of the electric field,  $(\mathbf{x}_i^{ant} - \mathbf{x}_{sh}^{gen}) \times [(\mathbf{x}_i^{ant} - \mathbf{x}_{sh}^{gen}) \times \mathbf{p}_\nu^{gen}]$ . Figure 3.5 illustrate angles  $\theta_i^{gen}$  and  $\alpha_i^{gen}$ .

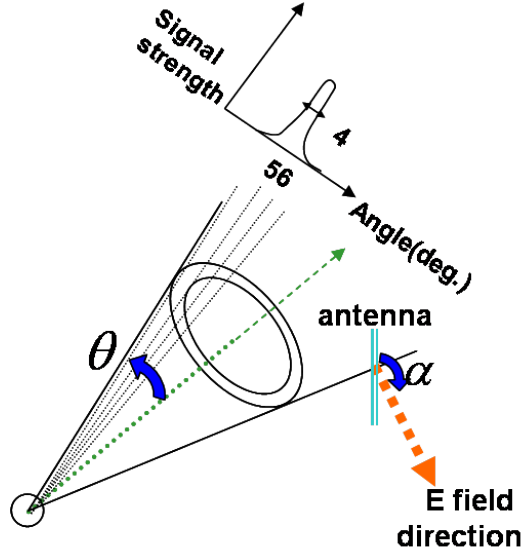


Figure 3.5: *Illustration of a radio Cherenkov wave, from the shower location to the antenna.*

The travel time of this signal is

$$t_i^{real} = \frac{\sqrt{(x_{sh}^{gen} - x_i^{ant})^2}}{c}, \quad (3.8)$$

where  $c$  is the speed of light divided by the refraction index of ice.

At the signal receiving end, the oscilloscope has time bin of 0.39 ns, and the time window is 100 ns. Noise before circuit has Gaussian distribution with mean voltage of 0 and  $\sigma_{noise}$  0.035 mV, whereas the trigger thresholds are that the Cherenkov cone intersects with the antenna and the attenuated signal must be larger than  $7\sigma_{noise}$ . An sample waveform is shown in Fig. 3.6: an originally bipolar waveform (like Fig. 3.4) magnified by a factor of signal strength  $V_i^{real}$ , shifted to the right by a time lag of  $t_i$ , and then added with noise.

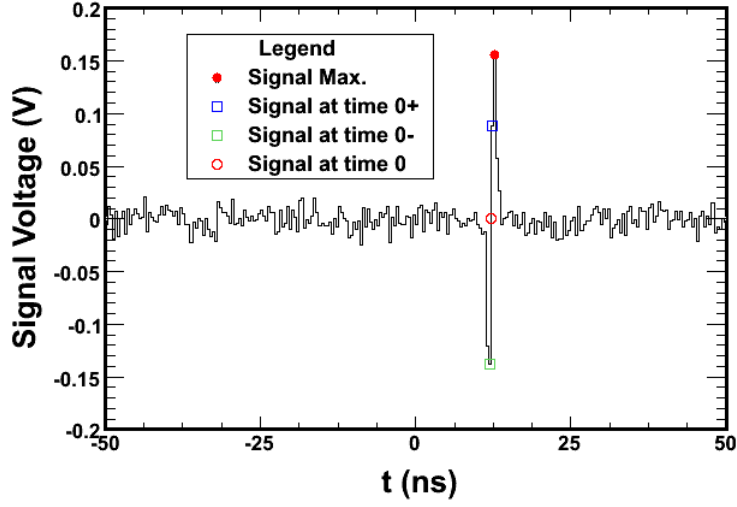


Figure 3.6: *An example waveform with noise.*

### 3.4 Determination of Arrival Time Difference and Pulse Voltage

To do the reconstruction of the events in the next stage, we have to extract arrival time difference,  $\Delta t_i^{obs}$ , and the pulse voltage,  $V_i^{obs}$ , from the waveform of each triggered antenna.

The time when the signal arrives at the antennas should be precisely determined, and then with the difference of arrival time between any two antennas, and with the requirement that at least four antennas must be triggered, the shower location can be obtained through the process of fitting. One way can be applied to calculate arrival time,  $t_i^{obs}$ , for each antenna is the use of the point where  $V = 0$  between the maximum and the minimum amplitudes, as shown in Fig. 3.6.

From the procedure described in the previous paragraph, for each antenna we

can obtain an arrival time. Arrival time difference, which is the information actually used in the reconstruction, is the arrival time subtracted by the reference of the arrival time,  $t_0^{obs}$ , which is defined as the arrival time for the antenna receiving the strongest signal among all antennas. Therefore,

$$\Delta t_i^{obs} = t_i^{obs} - t_0^{obs}. \quad (3.9)$$

As for  $V_i^{obs}$ , it is either the maximum point or the minimum point, depending on which one arrived at the antenna first.

### 3.5 Reconstruction of Neutrino Moving Directions

Our event reconstruction procedure is divided into two stages. The first stage is the reconstruction of shower location,  $\mathbf{x}_{sh}^{gen}$ . In this stage, the needed information is the arrival time difference,  $\Delta t_i^{obs}$  for each antenna. We set up a  $\chi^2$  formula:

$$\chi_1^2 = \sum_{i \text{ for all triggered antennas}} \frac{(\Delta t_i^{obs} - \Delta t_i^{hyp})^2}{\sigma_t^2}, \quad (3.10)$$

where  $\Delta t_i^{hyp}$  is the hypothesized arrival time difference, defined as

$$\begin{aligned} \Delta t_i^{hyp} &= t_i^{hyp} - t_0^{hyp} \\ &= \frac{\sqrt{(\mathbf{x}_{sh}^{hyp} - \mathbf{x}_i^{ant})^2}}{c} - \frac{\sqrt{(\mathbf{x}_{sh}^{hyp} - \mathbf{x}_0^{ant})^2}}{c}. \end{aligned} \quad (3.11)$$

By minimizing  $\chi_1^2$ , the best fit  $\mathbf{x}_{sh}^{rec}$  can be found, where a grid search is employed. Local minima of  $\chi_1^2$  value in the hypothesized-variable space is a serious problem and prohibit us from using other efficient ways to find the global minimum.

In the second stage of reconstruction, we still use  $\chi^2$  to find the best-fit. In this stage, the moving direction of neutrinos,  $\mathbf{p}_\nu^{gen}$ , is to be reconstructed, and the needed information is the pulse voltage received in each antenna. Furthermore, we also have to input the reconstructed shower location,  $\mathbf{x}_{sh}^{rec}$ , which is obtained in the first stage of reconstruction. Otherwise, we have to treat it as an unknown parameter to be reconstructed and this would intensively increase the computing time. The  $\chi^2$  formula in the second stage is given as

$$\chi_2^2 = \sum_{i \text{ for all triggered antennas}} \frac{(V_i^{obs} - V_i^{hyp})^2}{\sigma_V^2}, \quad (3.12)$$

where  $V_i^{hyp}$  is the hypothesized pulse voltage, which is defined as

$$\begin{aligned} V_i^{hyp}(\mathbf{x}_{sh}^{rec}, V_0^{hyp}, \mathbf{p}_\nu^{hyp}) = & V_0^{hyp} \\ & \cdot \frac{D_0}{\sqrt{(\mathbf{x}_{sh}^{rec} - \mathbf{x}_i^{ant})^2}} \cdot e^{\sqrt{(\mathbf{x}_{sh}^{rec} - \mathbf{x}_i^{ant})^2}/L_{att}^{ice}} \\ & \cdot a \cdot e^{-(\theta_i^{hyp} - 56^\circ)^2/2\sigma^2} \\ & \cdot \sin\alpha_i^{hyp} \text{ for Hpol antenna, or } \cos\alpha_i^{hyp} \text{ for Vpol antenna.} \end{aligned} \quad (3.13)$$

where  $\mathbf{p}_\nu^{hyp}$  is  $(1, \theta_\nu^{hyp}, \theta_\nu^{hyp})$  in spherical coordinate,  $\theta_i^{hyp}$  is the separation angle between the vector  $\mathbf{p}_\nu^{hyp}$  and the vector  $\mathbf{x}_i^{ant} - \mathbf{x}_{sh}^{rec}$ , and  $\alpha_i^{hyp}$  is the separation angle between the direction vector of the antenna  $i$ ,  $(x, y, z) = (0, 0, 1)$  and the direction vector of the electric field,  $(\mathbf{x}_i^{ant} - \mathbf{x}_{sh}^{rec}) \times [(\mathbf{x}_i^{ant} - \mathbf{x}_{sh}^{rec}) \times \mathbf{p}_\nu^{hyp}]$ . By minimizing  $\chi_2^2$ , the best fit  $\mathbf{p}_\nu^{rec} = (1, \theta_\nu^{rec}, \theta_\nu^{rec})$  can be found.

# Chapter 4

## Results

### 4.1 Resolutions of Arrival Time Difference and Pulse

#### Voltage

Figure 4.1 shows the resolution of time, where  $\Delta t = \Delta t_i^{obs} - \Delta t_i^{real} = (t_i^{obs} - t_0^{obs}) - (\Delta t_i^{real} - \Delta t_0^{real})$ , where antenna index  $i$  can be any triggered antenna, and index 0 stands for the reference antenna, the one receiving the strongest pulse in an event.

On the other hand, resolution of voltage is presented in Fig. 4.2, where  $\Delta V = V_i^{obs} - V_i^{real}$ . These two studies demonstrate that the code for the determination of arrival time differences and pulse voltages are correct, which play important roles in the reconstruction of the shower locations and neutrino moving directions.

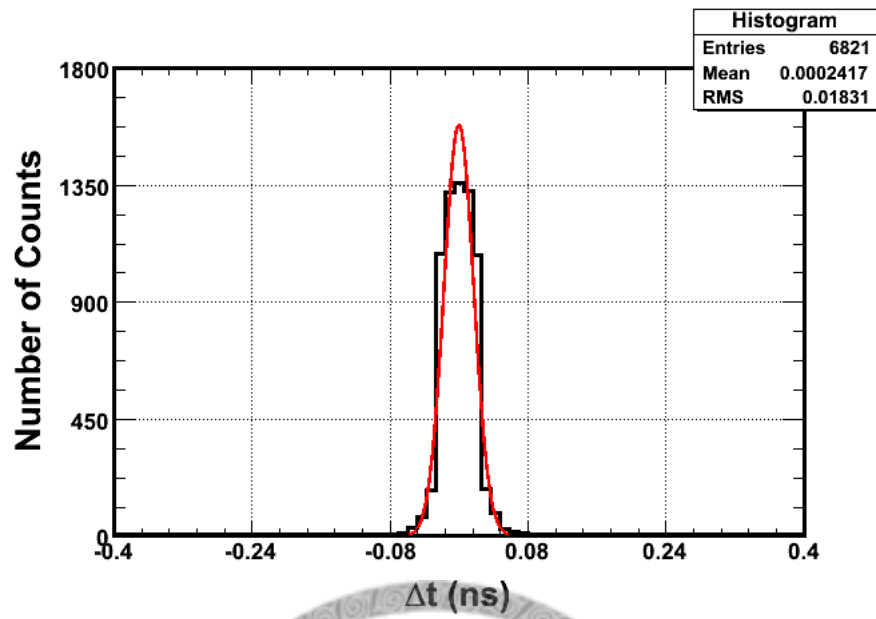


Figure 4.1: *Resolution of time.*

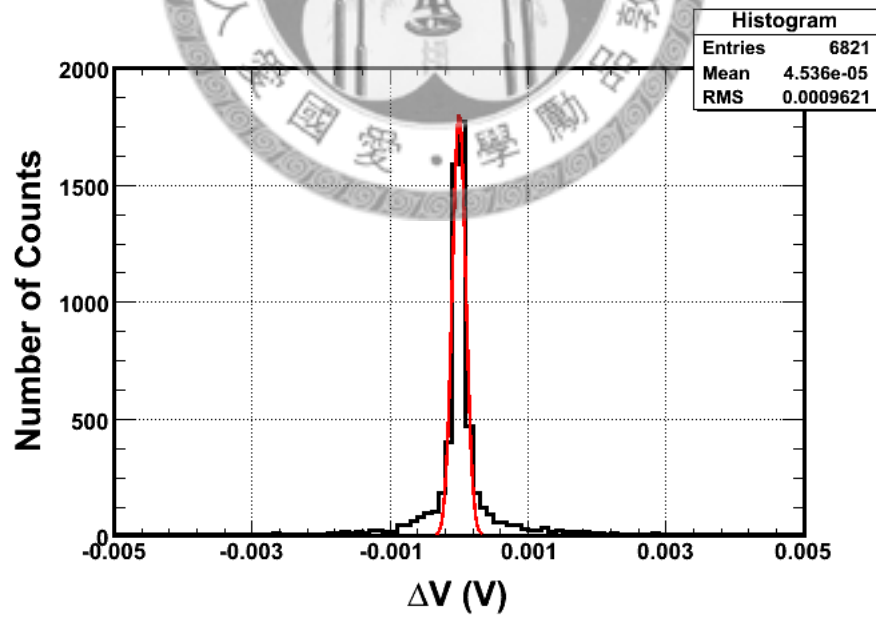


Figure 4.2: *Resolution of voltage.*



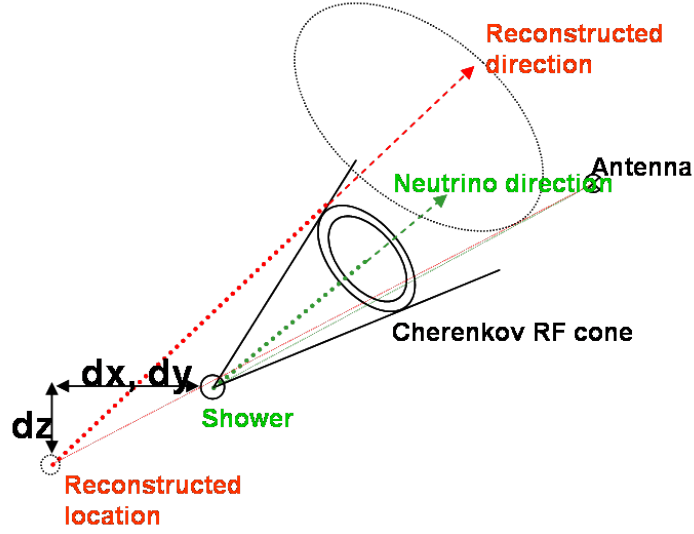


Figure 4.3: Illustration of the reconstructed shower location (in red) and the generated one (in green).

## 4.2 Resolutions of Shower Location, RF Wave Direction, and Neutrino Moving Direction

With Eqs. 3.10 and 3.11, the shower location can be reconstructed. Figure 4.3 illustrates the relation between the reconstructed shower location (in red) and the generated one (in green). The obtained resolutions of the shower location, 0.143 km in x axis, 0.098 km in y axis, 0.07 km in z axis, are shown in Figs. 4.4 to 4.6, which are the distributions of  $\Delta x = x_{sh}^{rec} - x_{sh}^{gen}$ ,  $\Delta y = y_{sh}^{rec} - y_{sh}^{gen}$ , and  $\Delta z = z_{sh}^{rec} - z_{sh}^{gen}$ .

Once the reconstructed shower locations are obtained, these reconstructed locations are taken as input in Eqs. 3.12 and 3.13 for the reconstruction of neutrino moving directions.

Figure 4.7 illustrate an example of the reconstructed RF wave direction (in red)

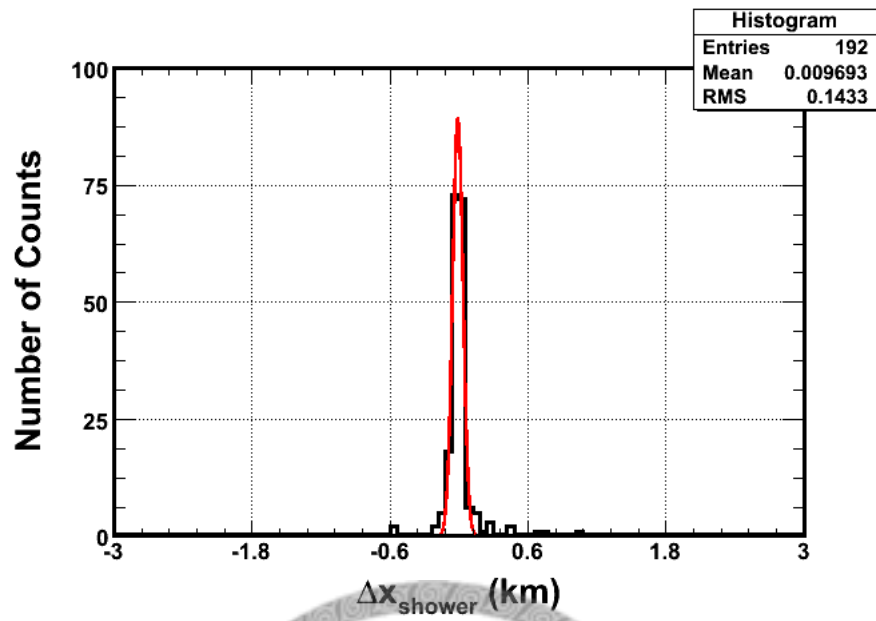


Figure 4.4: Resolution of shower location in  $x$  axis.

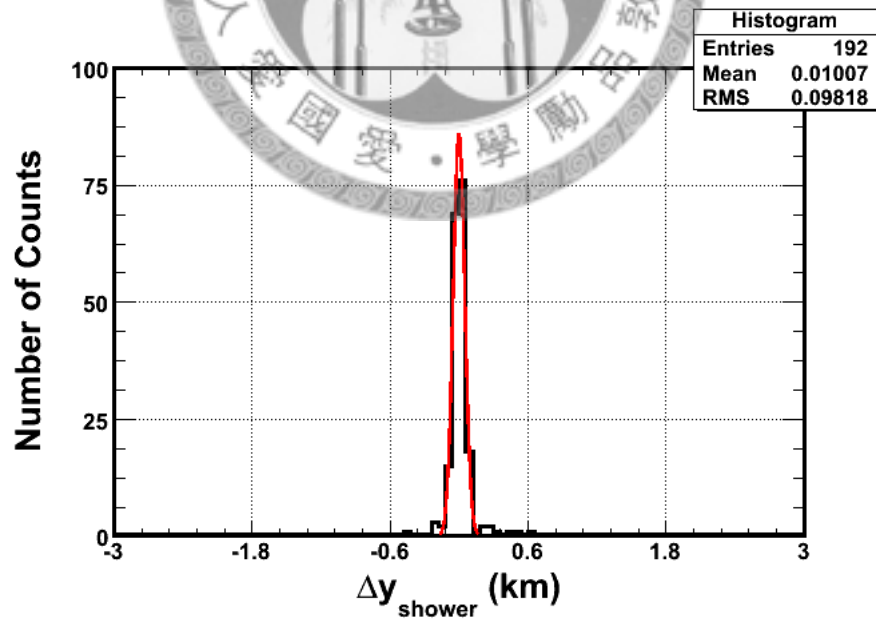


Figure 4.5: Resolution of shower location in  $y$  axis.

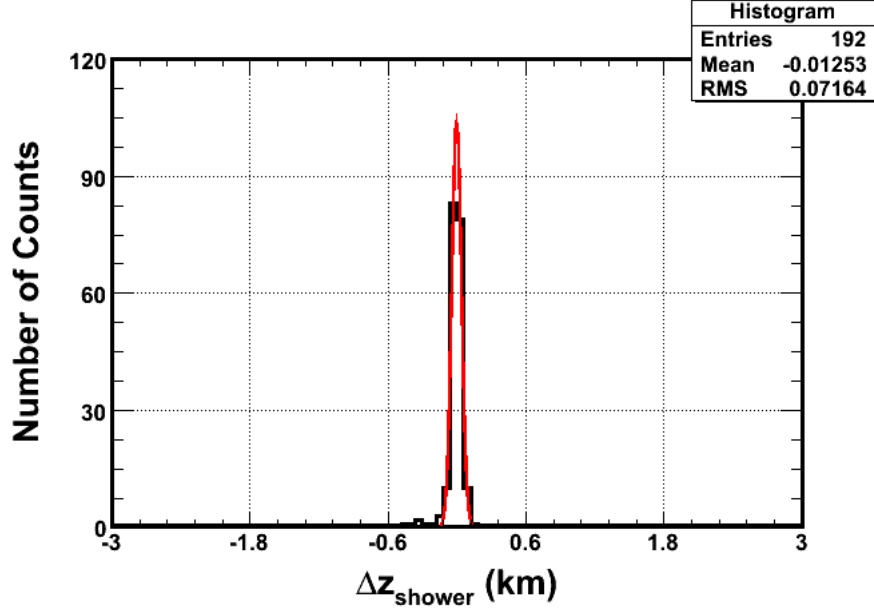


Figure 4.6: *Resolution of shower location in z axis.*

and the real one (in green). The obtained resolutions, in  $\theta$  direction  $1.45^\circ$ , and in  $\phi$  direction  $3.69^\circ$ , are shown in Figs. 4.8 and 4.9, which are the distributions of  $\Delta\theta_{RF} = \theta_{RF}^{rec} - \theta_{RF}^{gen}$ , and  $\Delta\phi_{RF} = \phi_{RF}^{rec} - \phi_{RF}^{gen}$ . The  $\theta$  and  $\phi$  here are the zenith angle and the azimuthal angle of the spherical coordinate with origin defined as the location of the antenna receiving the strongest signal, and z axis as before.

After the shower location and the RF wave direction are obtained, one can compute the neutrino direction according to Eqs. 3.12 and 3.13. Figure 4.10 illustrates the reconstructed neutrino moving direction (in red) and the generated one (in green). The obtained resolutions, in  $\theta$  direction  $4.88^\circ$ , and in  $\phi$  direction  $3.76^\circ$ , are shown in Figs. 4.11 and 4.12, which are the distributions of  $\Delta\theta_\nu = \theta_\nu^{rec} - \theta_\nu^{gen}$ , and  $\Delta\phi_\nu = \phi_\nu^{rec} - \phi_\nu^{gen}$ . The average of the separation angle between the generated  $\nu$  direction and the reconstructed one is shown in Fig. 4.13, which is  $2.38^\circ$ .

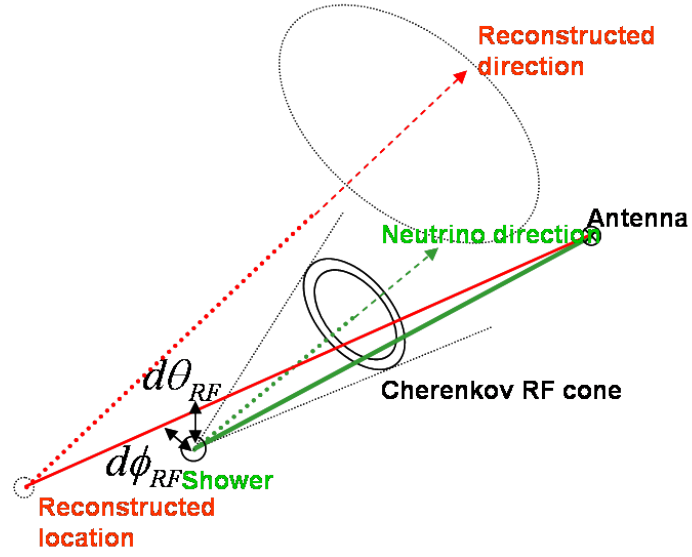


Figure 4.7: Illustration of the reconstructed RF wave direction (in red) and the generated one (in green).

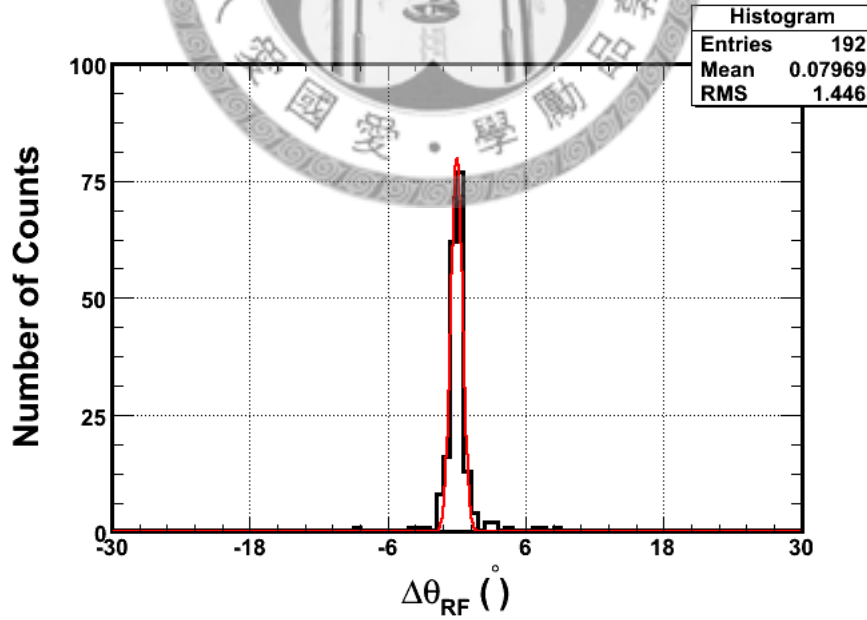


Figure 4.8: Resolution of RF wave direction in zenith angle.

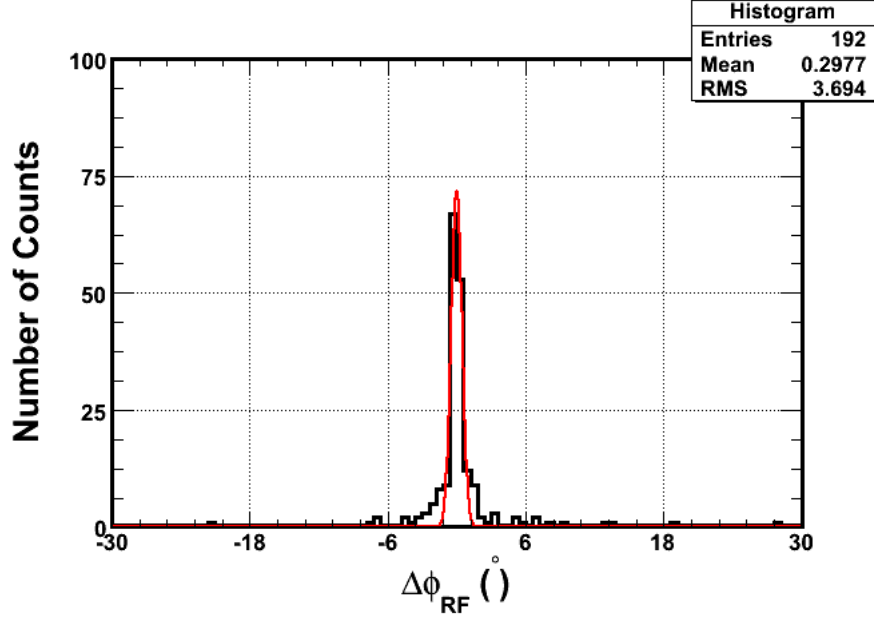


Figure 4.9: *Resolution of RF wave direction in azimuthal angle.*

The average of this angle is taken for the comparison of the neutrino angular resolution in this analysis because the separation angles are always positive, and thus the RMS value may not represent a proper indication of resolution. Note that  $\theta$  and  $\phi$  here are the zenith angle and the azimuthal angle of the spherical coordinate with the origin defined as the location of ARA center, and z axis as before. As mentioned before, the results presented so far have employed the ARA array geometry of station spacing as 1.33 km and antenna spacing as 30 m.

### 4.3 Optimization of ARA

To optimize the ARA, 16 different antenna spacings and 10 different station spacings are selected for the study on the resolution of the neutrino moving direction and the detection efficiency along with studies of noise effect. The optimum would be

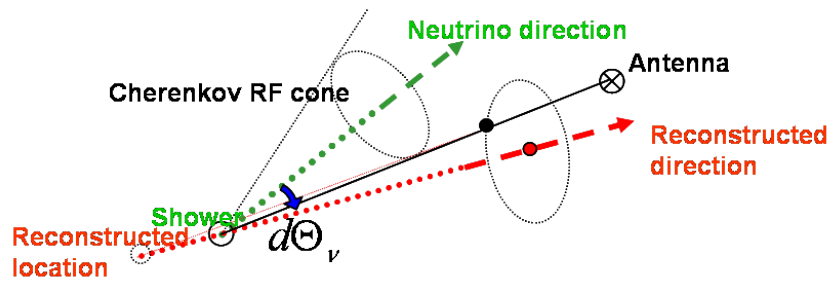


Figure 4.10: Illustration of the reconstructed neutrino moving direction (in red) and the generated one (in green).

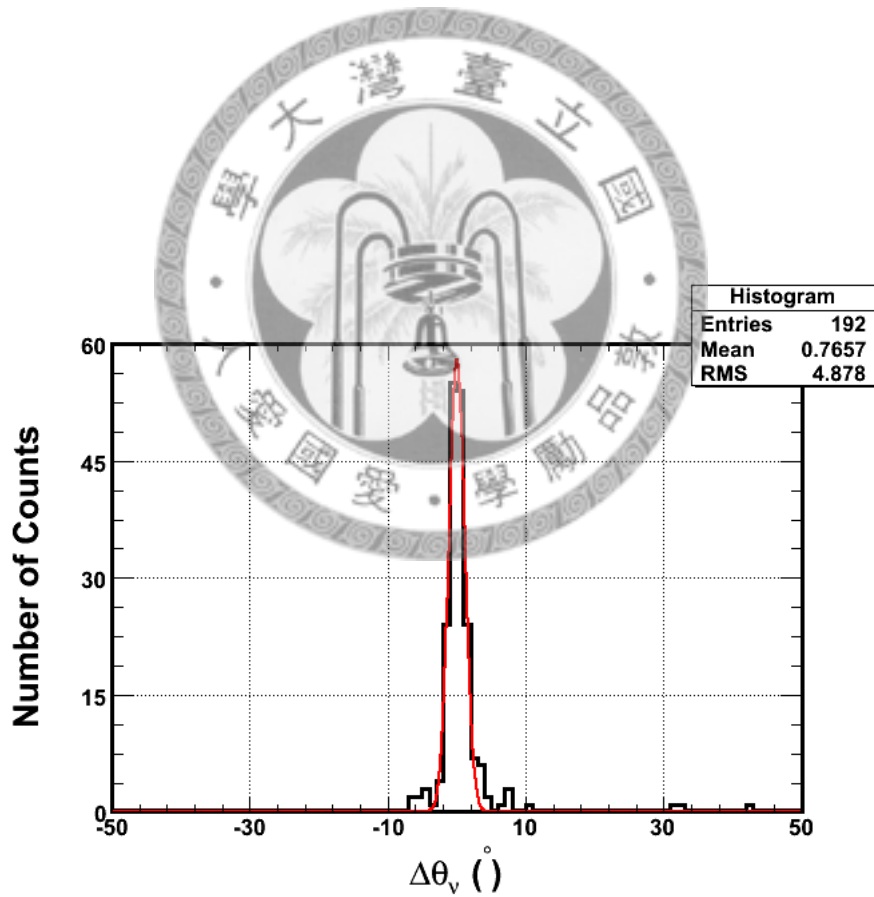


Figure 4.11: Resolution of neutrino moving direction in zenith angle.

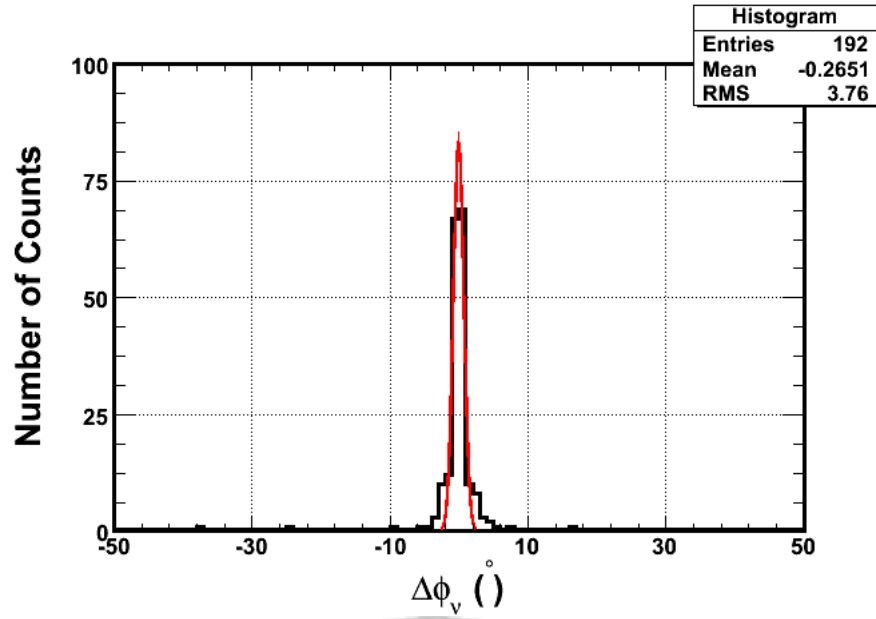


Figure 4.12: *Resolution of neutrino moving direction in azimuthal angle.*

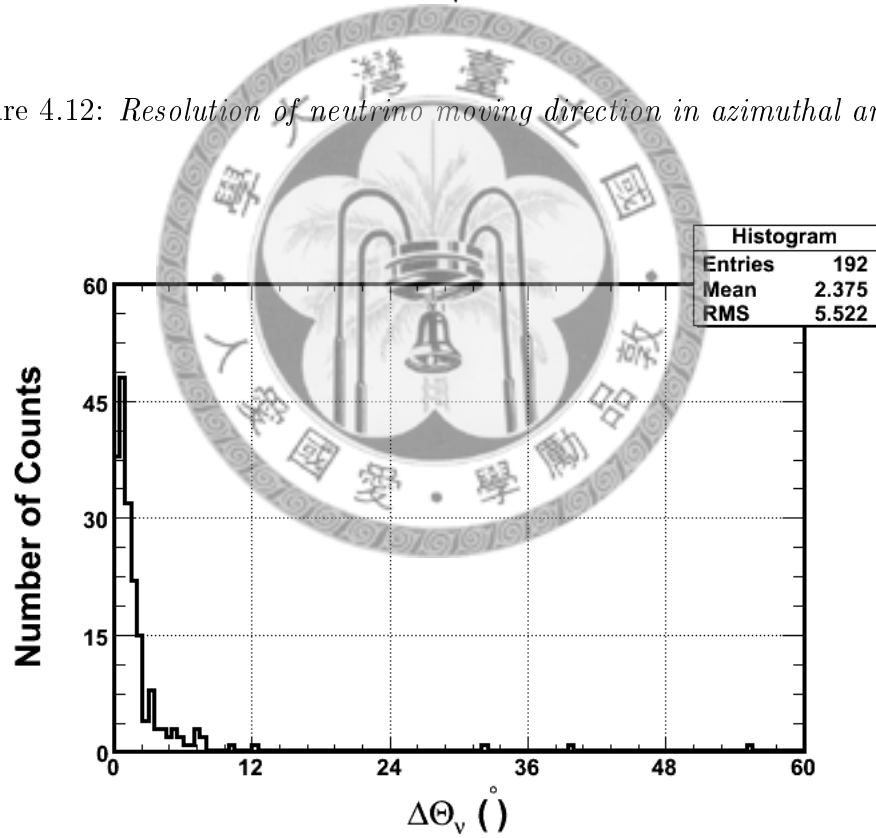


Figure 4.13: *Distribution of the separation angle between the generated  $\nu$  direction and the reconstructed one. The average of this angle is taken for the comparison of the neutrino angular resolution in this analysis.*

achieved when the resolution of the neutrino moving direction, i.e.  $\langle \Delta\Theta_\nu \rangle$ , is as good as possible, and the detection efficiency is as high as possible. The detection efficiency is defined as the number of triggered events that pass the trigger threshold divided by the total number of generated events in the cylinder volume, where the threshold applied to the pulse voltage is  $7 \sigma_{noise}$ .





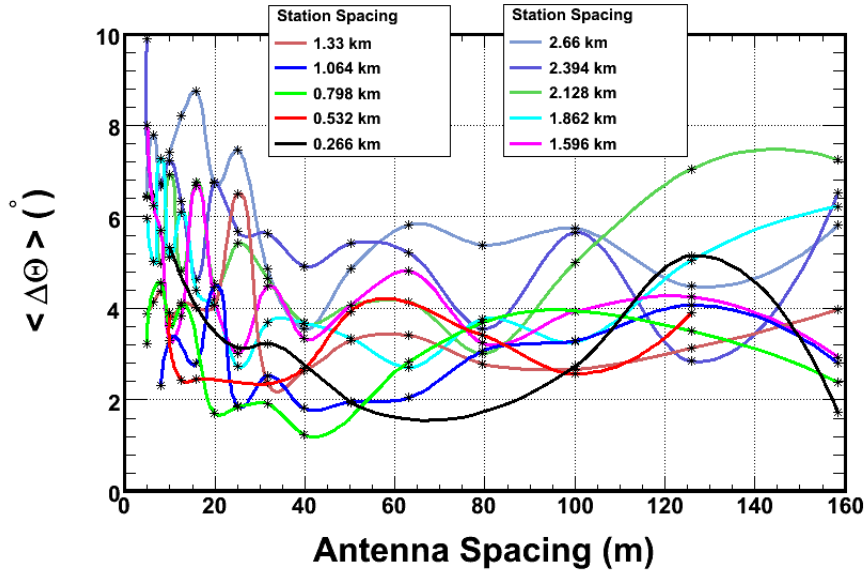


Figure 4.14: Resolutions of neutrino direction,  $\langle \Delta\Theta_\nu \rangle$ , versus antenna spacings and station spacings.

The antenna spacing varies from  $10^{0.7}$  m to  $10^{2.2}$  m in steps of 0.1 in the power index of 10. The station spacing changes from  $1.33\text{km}/5$  to  $1.33\text{km} \times 2$  in steps of  $1.33\text{km}/5$ . Note that the antenna spacing means the distance from the top antenna to the bottom one. The vertical spacings between any two antennas are the same, and the center of the four antennas in a borehole is located at the depth of 200 m. In addition, the side of the equilateral triangle in a station is set the same as the antenna spacing.

The mean value of the separation angles  $\langle \Delta\Theta_\nu \rangle$  versus the antenna spacings are shown in Figs. 4.14 and 4.15 in different displays, whereas the detection efficiencies versus the antenna spacings are given in Fig. 4.16.

Figs. 4.14, 4.15, and 4.16 suggest that  $\langle \Delta\Theta_\nu \rangle$  can be less than  $5^\circ$  if the station

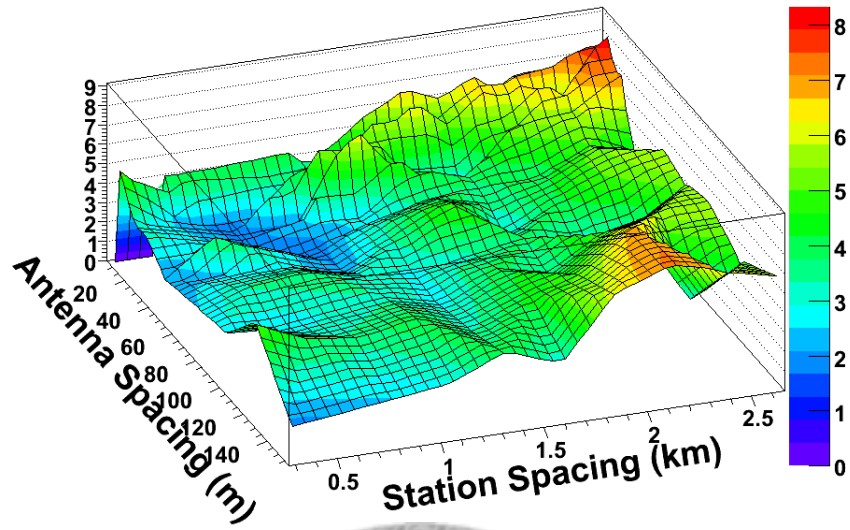


Figure 4.15: 3D display of resolutions of neutrino direction,  $\langle \Delta\Theta_\nu \rangle$  (in unit of degree), versus antenna spacings and station spacings.

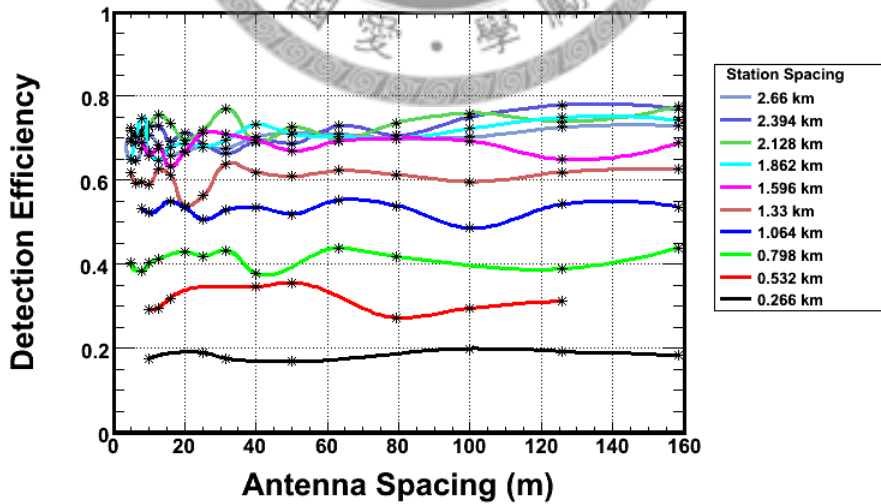


Figure 4.16: Detection efficiencies versus antenna spacings and station spacings.

spacing is set in the range of 1.33 km to 1.9 km and the antenna spacing is set in the range of 40 m to 100 m. One may notice that the detection efficiency reach a saturated value,  $\sim 70\%$ , when the station spacing is grater than  $\sim 1.5\text{km}$ .

To finalize the optimal choice for the ARA geometry, the effects of different noise levels added to the original waveform and different trigger thresholds are studied, too. The value of  $\sigma_{noise}$  is set at 0.035 mV for all analysis presented so far with  $V_0^{gen}$  varying in the range of 0 to 5 V. In the following studies of how the noise levels would affect the resolution of the neutrino moving direction, in each case a different level of noise added to the waveform is assumed, i.e.  $\sigma'_{noise} = \alpha\sigma_{noise}$ , with  $\alpha$  greater than one, whereas  $V_0^{gen}$  is fixed at 5 V. Different trigger thresholds are applied:  $V_i^{obs} > 3.5\sigma_{noise}$ ,  $V_i^{obs} > 5\sigma_{noise}$ ,  $V_i^{obs} > 7\sigma_{noise}$ . For these studies, only 100 events are generated in each case. The results of  $\langle\Delta\Theta_\nu\rangle$  and the detection efficiency versus the noise level under different trigger thresholds are presented in Figs. 4.17 to 4.34 for different antenna spacings and different station spacings. It was found that the larger  $\sigma'_{noise}$  added to the waveforms, the worse the resolution of the neutrino moving direction, which is as expected. In addition, the higher the trigger threshold, the lower the detection efficiency.

In summary, with the noise effect taken into account, in order to make the resolution of the neutrino moving direction as good as possible and detection efficiency as high as possible, the optimal choice for ARA geometry would be 1.6 km for the station spacing and 40 m for the antenna spacing.

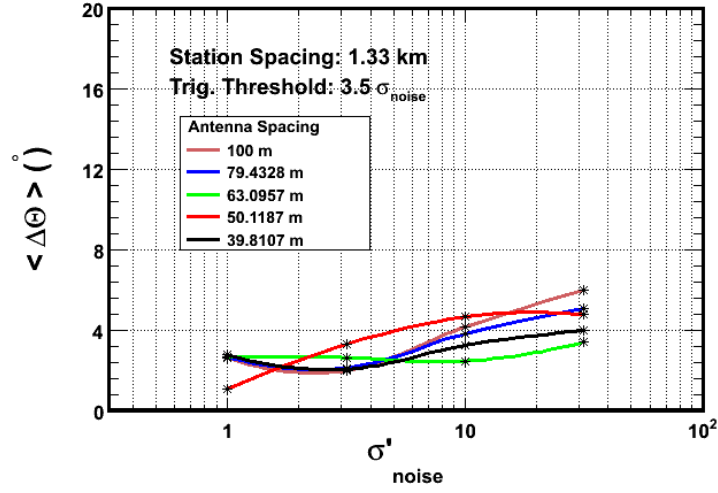


Figure 4.17: Resolutions of neutrino direction,  $\langle \Delta\Theta_\nu \rangle$ , versus different noise levels and antenna spacings, where the station spacing is set at 1.33 km and the trigger threshold is  $3.5\sigma_{noise}$ .

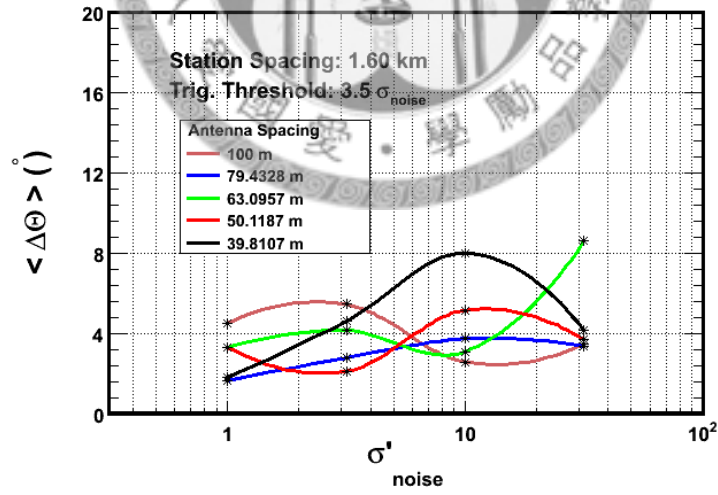


Figure 4.18: Resolutions of neutrino direction,  $\langle \Delta\Theta_\nu \rangle$ , versus different noise levels and antenna spacings, where the station spacing is set at 1.60 km and the trigger threshold is  $3.5\sigma_{noise}$ .

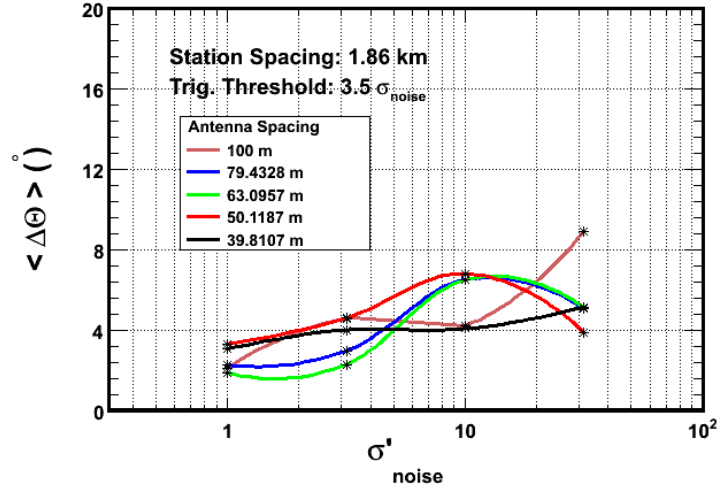


Figure 4.19: Resolutions of neutrino direction,  $\langle \Delta\Theta \rangle$ , versus different noise levels and antenna spacings, where the station spacing is set at 1.86 km and the trigger threshold is  $3.5\sigma_{noise}$ .

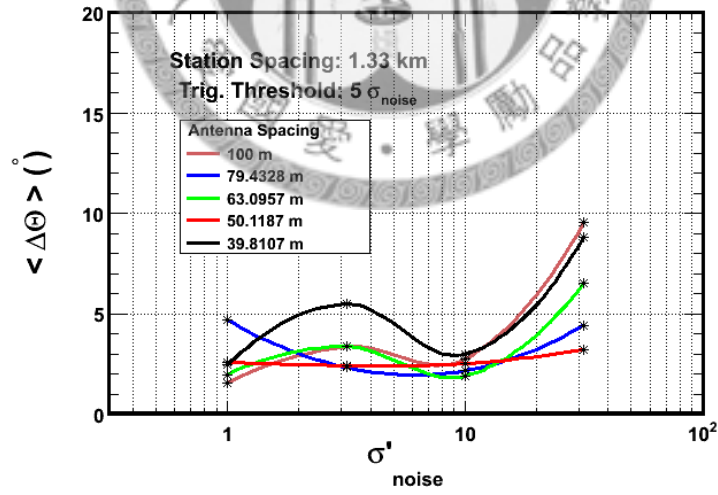


Figure 4.20: Resolutions of neutrino direction,  $\langle \Delta\Theta \rangle$ , versus different noise levels and antenna spacings, where the station spacing is set at 1.33 km and the trigger threshold is  $5\sigma_{noise}$ .

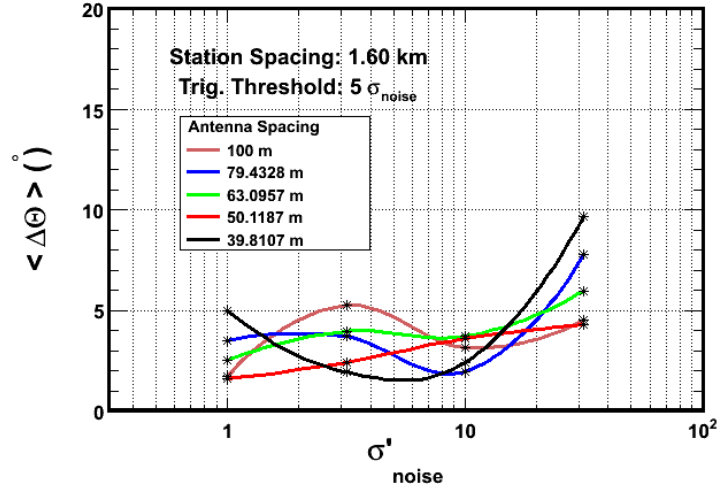


Figure 4.21: Resolutions of neutrino direction,  $\langle \Delta\Theta_\nu \rangle$ , versus different noise levels and antenna spacings, where the station spacing is set at 1.60 km and the trigger threshold is  $5\sigma_{noise}$ .

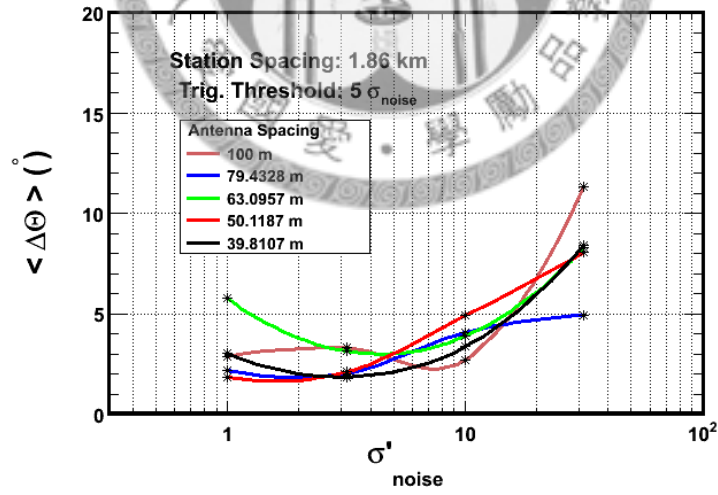


Figure 4.22: Resolutions of neutrino direction,  $\langle \Delta\Theta_\nu \rangle$ , versus different noise levels and antenna spacings, where the station spacing is set at 1.86 km and the trigger threshold is  $5\sigma_{noise}$ .

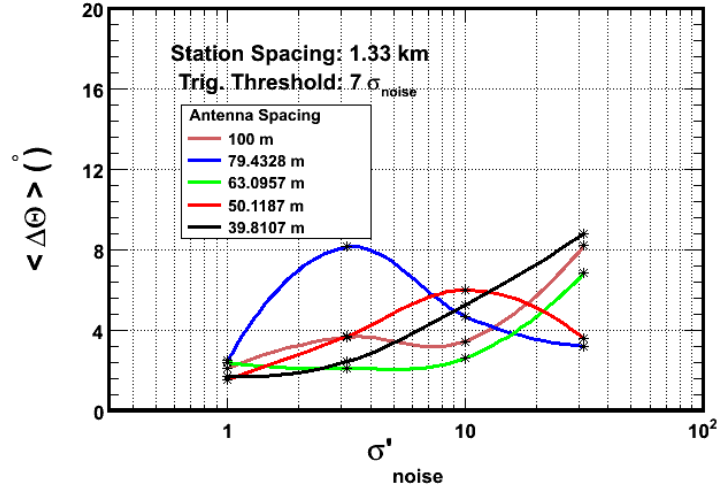


Figure 4.23: Resolutions of neutrino direction,  $\langle \Delta\Theta_\nu \rangle$ , versus different noise levels and antenna spacings, where the station spacing is set at 1.33 km and the trigger threshold is  $7\sigma_{noise}$ .

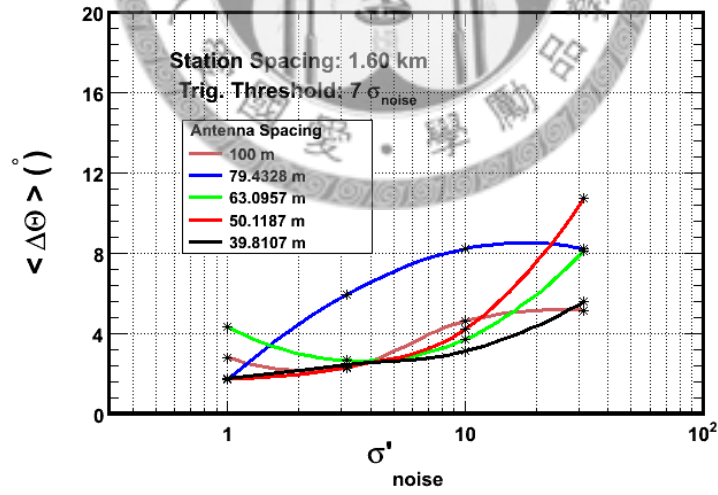


Figure 4.24: Resolutions of neutrino direction,  $\langle \Delta\Theta_\nu \rangle$ , versus different noise levels and antenna spacings, where the station spacing is set at 1.60 km and the trigger threshold is  $7\sigma_{noise}$ .

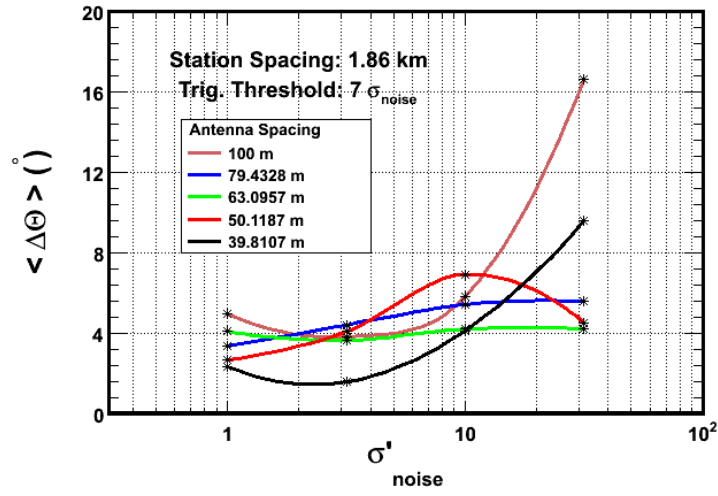


Figure 4.25: Resolutions of neutrino direction,  $\langle \Delta\Theta_{\nu} \rangle$ , versus different noise levels and antenna spacings, where the station spacing is set at 1.86 km and the trigger threshold is  $7\sigma_{noise}$ .

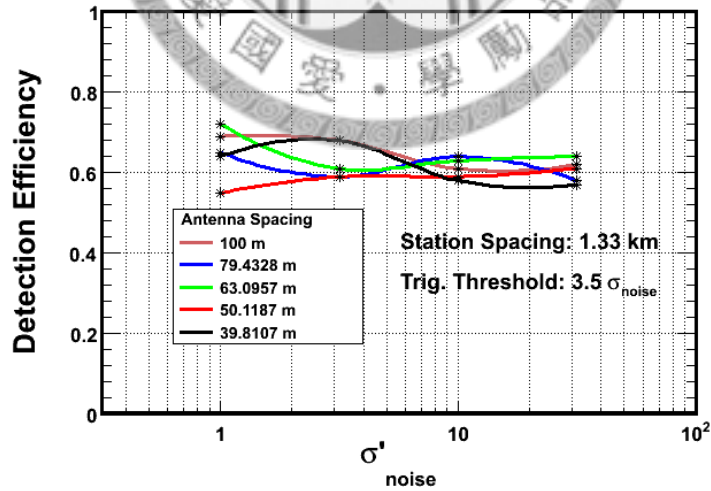


Figure 4.26: Detection Efficiencies versus different noise levels and antenna spacings, with the station spacing of 1.33 km and the trigger threshold is  $3.5\sigma_{noise}$ .



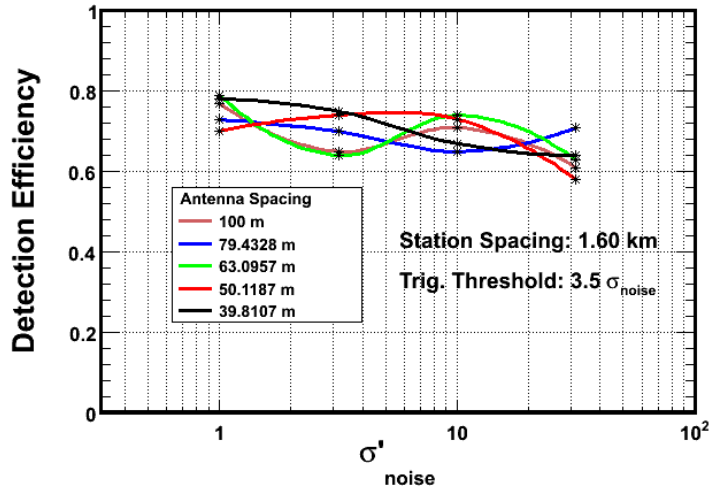


Figure 4.27: *Detection Efficiencies versus different noise levels and antenna spacings, with station spacing as 1.60 km and the trigger threshold is  $3.5\sigma_{noise}$ .*

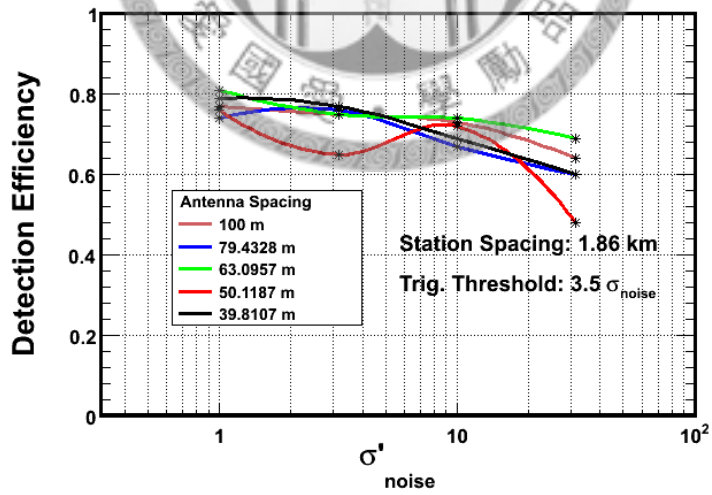


Figure 4.28: *Detection Efficiencies versus different noise levels and antenna spacings, with station spacing as 1.86 km and the trigger threshold is  $3.5\sigma_{noise}$ .*

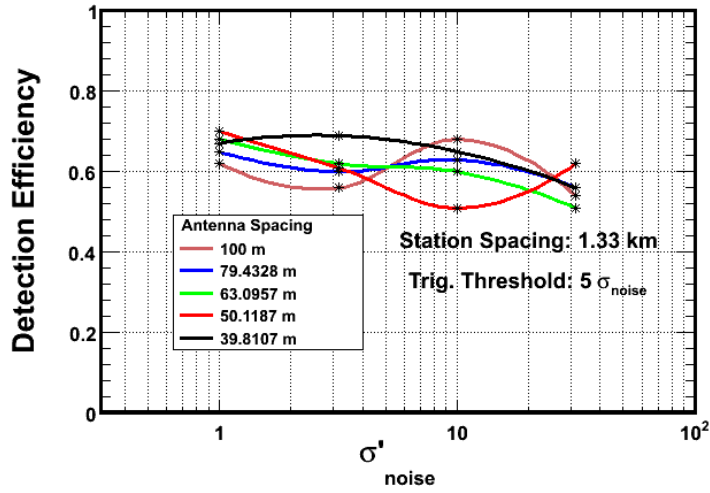


Figure 4.29: *Detection Efficiencies versus different noise levels and antenna spacings, with the station spacing of 1.33 km and the trigger threshold is  $5\sigma_{noise}$ .*

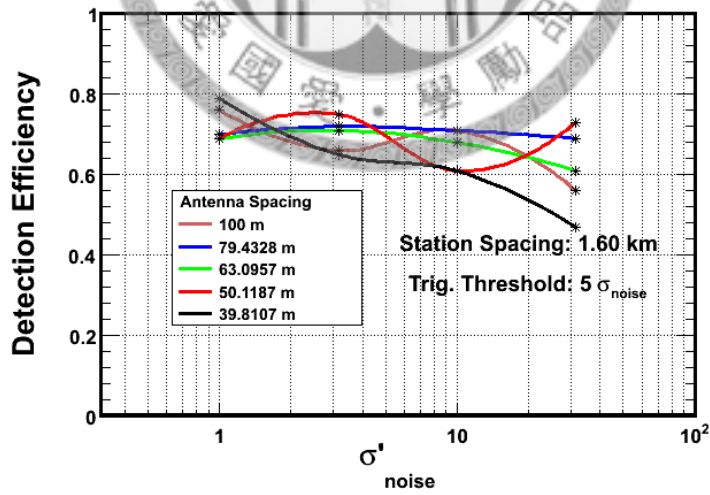


Figure 4.30: *Detection Efficiencies versus different noise levels and antenna spacings, with station spacing as 1.60 km and the trigger threshold is  $5\sigma_{noise}$ .*

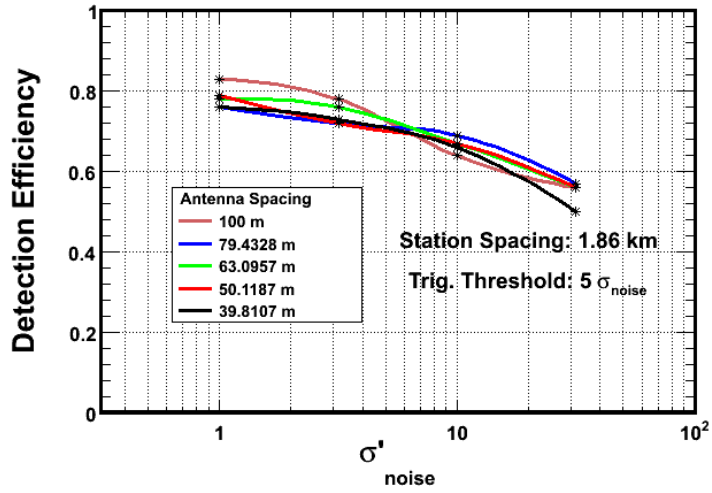


Figure 4.31: *Detection Efficiencies versus different noise levels and antenna spacings, with station spacing as 1.86 km and the trigger threshold is  $5\sigma_{noise}$ .*

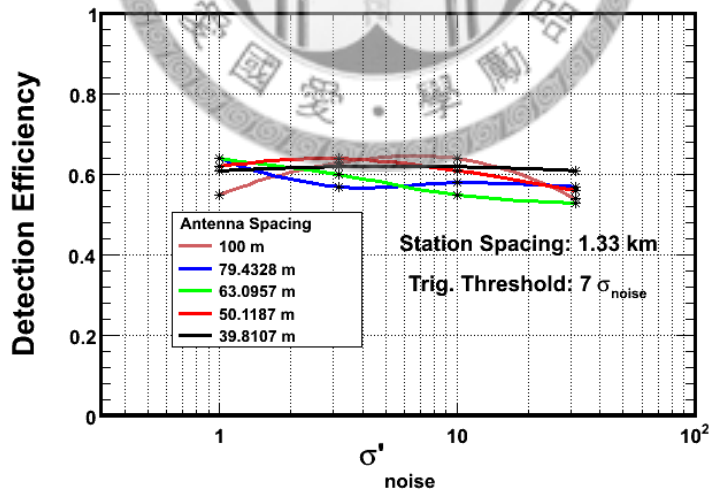


Figure 4.32: *Detection Efficiencies versus different noise levels and antenna spacings, with the station spacing of 1.33 km and the trigger threshold is  $7\sigma_{noise}$ .*

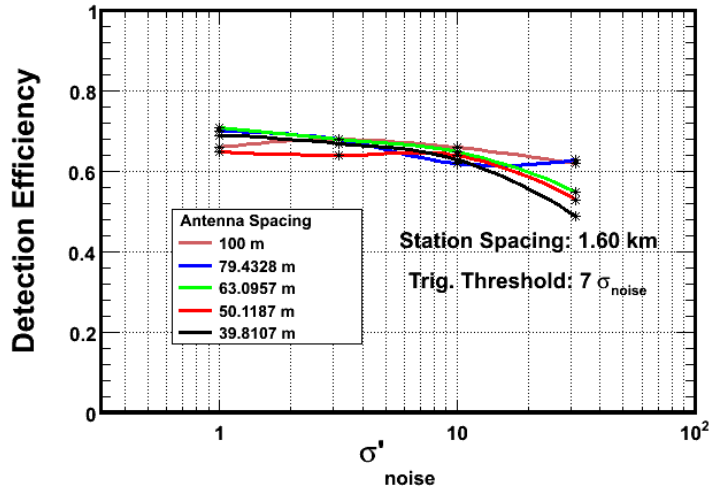


Figure 4.33: *Detection Efficiencies versus different noise levels and antenna spacings, with station spacing as 1.60 km and the trigger threshold is  $7\sigma_{noise}$ .*

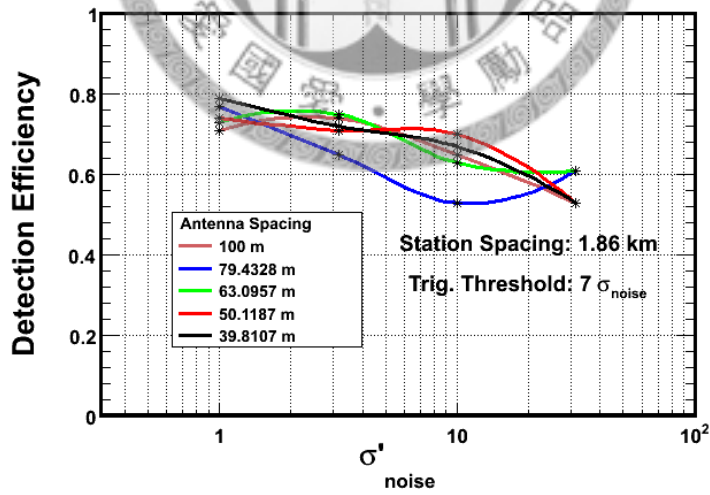


Figure 4.34: *Detection Efficiencies versus different noise levels and antenna spacings, with station spacing as 1.86 km and the trigger threshold is  $7\sigma_{noise}$ .*

# Chapter 5

## Summary

Angular Resolution of Neutrino Moving Direction: One of the main goals of ARA is to point back to cosmic accelerators through the determination of the UHE neutrino moving directions, so the resolution of it is particularly important.

To optimize the ARA, both the resolution of the neutrino moving direction and the detection efficiency should be considered. Basically, the detection efficiency increases as the station spacing gets larger. From Fig. 4.16, however, it reaches a plateau of  $\sim 70\%$  detection efficiency when the station spacing is greater than  $\sim 1.5$  km where the regions which each station can cover no longer overlap. With the noise effect taken into account, in order to make the resolution of the neutrino moving direction as good as possible and detection efficiency as high as possible, the optimal choice for ARA geometry would be 1.6 km for the station spacing and 40 m for the antenna spacing.

In the simulation of angular resolution of neutrino direction for Antarctic Ross Ice Shelf ANtenna Neutrino Array (ARIANNA) experiment, the resolution in  $\theta$

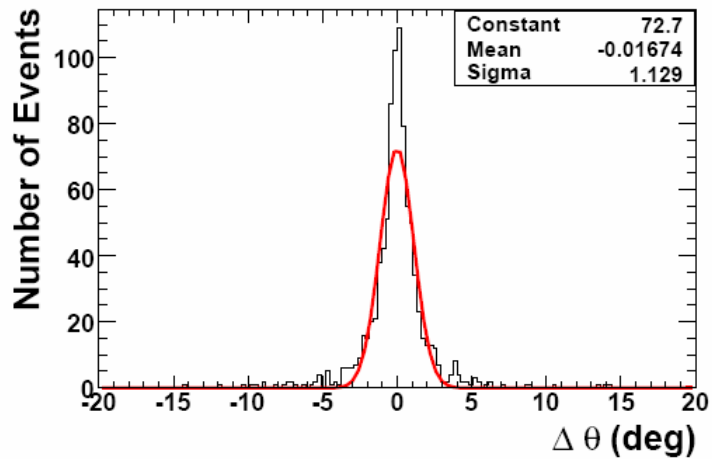


Figure 5.1: *Resolution of neutrino moving direction in  $\theta$  direction in the simulation for ARIANNA.*

direction is  $1.1^\circ$ , as shown in Fig. 5.1 [34]. However, to reach such a good resolution, ARIANNA has to build its array up to 11 stations per  $\text{km}^2$ , which means that its antenna density has to be 13 times greater than ARA if we set the station spacing as 1.33 km. Based on this comparing, the design of ARA is in a better balance point between the resolution and the cost.

In the future, if ARA can get more funding to increase the density of the antenna number, a much better resolution of neutrino moving direction can be achieved.

# Bibliography

- [1] I. A. Grenier and A. K. Harding, in Albert Einstein Century International Conference, Vol. 861 of American Institute of Physics Conference Series (American Institute of Physics, New York, 2006), pp. 630-637.
- [2] Antonio Codino, "The transition from tortuous to rectilinear cosmic ray trajectories in the Galaxy is at the origin of the knee and the ankle", 30th International Cosmic Ray Conference, 2007
- [3] Efimov N N et al 1991 ICRR Symp. on Astrophysical Aspects of the Most Energetic Cosmic Rays edMNagano and F Takahara (Singapore: World Scientific)
- [4] D.P. Torres and L.A. Anchordoqui, Rep. Prog. Phys., **67**, 1663-1730 (2004).
- [5] P. Bhattacharjee and G. Sigl, Phys.Rept. **327**, 109, (2000).
- [6] D. Seckel and T. Stanev, Phys. Rev. Lett **95**, 141101(2005)
- [7] K. Greisen, End to the cosmic ray spectrum?, Phys. Rev. Lett. 16, 748 (1966).
- [8] G. T. Zatsepin and V. A. Kuzmin, Upper limit of the spectrum of cosmic rays, JETP Lett. 4, 78 (1966).

- [9] V. S. Berezinsky and G. T. Zatsepin, Cosmic neutrinos of superhigh energy, *Yad. Fiz.* 11, 200 (1970).
- [10] F. W. Stecker, Ultrahigh energy photons, electrons and neutrinos, the microwave background, and the universal cosmic ray hypothesis, *Astrophys. Space Sci.* 20, 47 (1973).
- [11] O. E. Kalashev, V. A. Kuzmin, D. V. Semikoz and G. Sigl, "Ultra-high energy neutrino fluxes and their constraints," *Phys. Rev. D* 66, 063004 (2002).
- [12] R. J. Protheroe, and P. A. Johnson, *Astropart. Phys.* 4, 253 (1996).
- [13] M. Roth, for the Auger Collaboration, "Measurement of the UHECR energy spectrum using data from the Surface Detector of the Pierre Auger Observatory," Contribution to the 30th International Cosmic Ray Conference, Merida, Mexico, <http://arxiv.org/abs/0706.2096>, 2007.
- [14] A.V.Glushkov et al., *Astropart. Phys.* 4 (1995) 15.
- [15] D.J.Bird et al., *Astrophys. J.* 441 (1995) 144. J.W.Elbert, P.Sommers, *Astrophys. J.* 441 (1995) 151; Baltrusaitas, R.M., Cassiday, G.L., Elbert, J.W., et al., *Phys. Rev. D* 31, 2192 (1985).
- [16] S.Yoshida et al., *Astropart. Phys.* 3 (1995) 105; also Shigeru Yoshida, Hongyue Dai, (*astro-ph/9802294*). *Journal of Physics G* 24 (1998) 905.
- [17] R. U. Abbasi, et al., The HiRes Collaboration, (2007) submitted to *Phys. Rev. Lett.*, *astro-ph/0703099*.



- [18] M.A. Lawrence, R.J.O. Reid, A.A. Watson. J. Phys. G. 17 (1991) 733.
- [19] Antarctic Impulsive Transient Antenna collaboration
- [20] P. Gorham, 1st International Workshop on the Saltdome Shower Array (SalSA),  
SLAC, Feb 2005
- [21] G.A. Askaryan, JETP 14, 441 (1962).
- [22] P.W. Gorham et al. ANITA Collaboration, Phys. Rev. Lett. 99, 171101 (2007)
- [23] P. Chen and K.D. Hoffman, arXiv:0902.3288 [astro-ph] (2009).
- [24] Askaryan Radio Array Proposal, submitted to US NSF (2009).
- [25] A. Taylor and A. D. Castro and E. Castillo-Ruiz, arXiv:0902.3012v1
- [26] T. Stanev, arXiv:0810.2501v1
- [27] F. W. Stecker, Phys. Rev. Lett. 21, 1016 - 1018 (1968)
- [28] Particle Data Group, [http://pdgusers.lbl.gov/sbl/gammap\\_tatal.dat](http://pdgusers.lbl.gov/sbl/gammap_tatal.dat)
- [29] V.S. Berezhinsky and S.I. Grigo'eva, Astro. Astrophys. **199**, 1-12(1988)
- [30] R. Engel, D. Seckel and T. Stanev, Phys. Rev. D, **64**, 093010
- [31] A. MujLcke *et al.*, Comput. Phys. Commun. **124**, 290 (2000)
- [32] E. Waxman, Astrophys. J. Lett. **452**, L1 (1995)
- [33] P.W. Gorham *et al.*, Astropar. Phys.**32**, 10-41 (2009)

[34] F. Wu, J. Nam, Proceedings of the 30th International Cosmic Ray Conference  
(2007).

